Modeling and Simulations of the DSS 13 Antenna Control System

W. Gawronski and J. A. Mellstrom
Ground Antennas and Facilities Engineering Section

A model of the antenna control system for the azimuth and elevation axes of the DSS 13 antenna is developed. This model is used for simulation of elevation and azimuth dynamics, cross-coupled dynamics, and radio-frequency pointing error due to both input commands and wind disturbances. This model also serves as a tool for the antenna controller design. A modal state-space model of the antenna structure was obtained from its finite-element model with a free-rotating tipping structure and alidade. Model reduction techniques applied separately for the antenna structure, elevation and azimuth drives, and rate-loop model reduce the system order to one-third of that of the original, while preserving its significant dynamic properties. Extensive simulation results illustrate properties of the model.

I. Introduction

The control system model for the elevation drive of the DSS 13 antenna was described in [1]. This article extends the previous approach to the full control system of the antenna (in azimuth and elevation), and extends the structural model for modes up to 10 Hz. This article also describes the wind disturbance model used to study this important source of antenna pointing error. The antenna structural model for the 90-deg elevation angle is obtained from the antenna's finite-element model with a free rotation in azimuth and elevation. A linear structural model is analyzed. Nonlinear effects due to dry friction are not considered. A state-space model is used to describe the control system and its components.

The structure and the drives, as well as the rate-loop model, have some purely imaginary poles or poles at zero (the latter poles have integrating properties). Known reduction techniques fail when applied to systems with integrators. A balanced reduction technique, developed here for the systems with integrators, was applied to reduce the order of the structural model, elevation and azimuth drive models, and subsequently the rate-loop model. The order of the resulting reduced model is one-third of the original's, while the modeling error is small in comparison to the system dynamics.

The presented approach is an analytical base for computer software development. This software is designed as a tool for simulations of antenna dynamics due to the input commands and disturbances, for control system analysis, and for the position control algorithm design. Extensive simulations have been performed and described to illustrate the overall system properties.

II. Structural Model

The antenna structural model for elevation control purposes was described in [1]. In this article, structural modeling is expanded for the antenna in both elevation and azimuth motions. New developments specific to the joint azimuth and elevation modeling are presented; the reader is referred to [1] for the approaches used in the elevation control system model. The state-space representation denoted by a quadruple (A, B, C, D) is a set of first-order differential equations

$$\dot{x} = Ax + Bu, \qquad y = Cx + Du \tag{1}$$

where the state vector x is of dimension $n \times 1$, the input u is of dimension $p \times 1$, the output y is of dimension $q \times 1$, and the matrices A, B, C, and D are of dimensions $n \times n, n \times p, q \times n$, and $q \times p$, respectively.

A. Full Model

In this section the state-space quadruple in modal coordinates (A_s, B_s, C_s, D_s) for the antenna structure is determined. The state vector of the structure x_s consists of modal displacements q_s and modal velocities v_s,

$$x_s^T = [q_s^T \ v_s^T] \tag{2}$$

From the finite-element model, generated by the JPL-IDEAS code[1], $m = 21$ modes are obtained. The first and the second modes are rigid-body modes with zero natural frequency. The modes are determined for r selected points of interest; thus, $\phi_i = [\phi_{i1}, \phi_{i2}, \cdots, \phi_{ir}]^T, i = 1, \cdots, 21$. The antenna structural model is generated from the natural frequencies ω_i and mode shapes ϕ_i. Modal damping of the structure ζ_i is assumed to be $\zeta_i = 0.005$ for $i = 1, \cdots, 21$. The antenna structure is free to rotate about the elevation and azimuth axes.

1. Matrix A_S. Denote

$$\Omega = diag(\omega_i), \qquad Z = diag(\zeta_i), i = 1, 2, \cdots, m \tag{3}$$

then the system matrix A_s for the antenna structure is

$$A_s = \begin{bmatrix} 0 & I_m \\ -\Omega^2 & -2Z\Omega \end{bmatrix} \tag{4}$$

[1] R. Levy and D. Strain, *JPL-IDEAS Finite Element Analysis and Design Optimization Program*, Document NPO-17783 (internal document), Jet Propulsion Laboratory, Pasadena, California, October 1988.

where I_m is the identity matrix of dimensions $m \times m$. Details of the derivation of A_s are presented in [1]. Numerical values of Ω, Z, and other parameters are given in Appendix A.

2. Matrix C_S. The following outputs of the antenna structure are considered: elevation angle θ_e, elevation rate $\dot{\theta}_e$, elevation pinion rate $\dot{\theta}_{pe}$, azimuth angle θ_a, azimuth rate $\dot{\theta}_a$, azimuth pinion rates $\dot{\theta}_{pa1}$ and $\dot{\theta}_{pa2}$, pointing error angle in elevation ϵ_{el}, pointing error angle in cross-elevation ϵ_{xel}, and subreflector x, y, and z positions q_{sx}, q_{sy}, and q_{sz}. Thus, the antenna output matrix C_s consists of twelve rows:

$$C_s^T = [C_{s1}^T, C_{s2}^T, \cdots, C_{s11}^T, C_{s12}^T] \tag{5}$$

where

C_{s1} is the elevation encoder reading

C_{s2} is the elevation rate

C_{s3} is the elevation pinion rate

C_{s4} is the azimuth encoder reading

C_{s5} is the azimuth rate

C_{s6} and C_{s7} are azimuth pinion rates

C_{s8} and C_{s9} are the pointing errors in elevation and cross-elevation

C_{s10}, C_{s11}, and C_{s12} are the subreflector x, y, and z positions

The first two rows (the elevation angle and rate) are determined as follows. In the finite-element model, the node at the bull gear center has a label $nb = 5380$ and the node at distance R to nb has a label $nc = 41212$ (see Fig. 1). The high stiffness of the bull gear and the close location of the two nodes allows one to determine the elevation angle as a rigid-body rotation

$$\theta_e = \frac{y_{nc} - y_{nb}}{R} = \frac{(C_{ncy}\Phi - C_{nby}\Phi)q_s}{R} = \frac{(\phi_{ncy} - \phi_{nby})q_s}{R}$$

where R is the bull gear radius and C_{ncy} and C_{nby} denote row vectors with one nonzero element. The nonzero element of C_{ncy} is equal to 1 and is located in the position in q_s corresponding to the y displacement of node nc. The

nonzero element of C_{nby} is equal to 1 and is located in the position corresponding to the y displacement at node nb in the vector q_s. Thus, ϕ_{ncy} and ϕ_{nby} are

$$\phi_{ncy} = [\phi_{1ncy}, \cdots, \phi_{mncy}], \qquad \phi_{nby} = [\phi_{1nby}, \cdots, \phi_{mnby}]$$

where ϕ_{incy} is the ith mode component at node nc in the y direction and ϕ_{inby} is the ith mode component at node nb in the y direction. From this, it follows that:

$$C_{s1} = [0 \; C_{se}], \qquad C_{s2} = [C_{se} \; 0] \tag{6a}$$

where $C_{se} = (\phi_{ncy} - \phi_{nby})/R$.

For the determination of the pinion rate measurement matrix C_{s3}, denote the velocity at pinion housing v_p (at node nu), bull gear velocity v_b at node no (see Fig. 1), and their projections v_1 and v_2 onto a plane tangential to the bull gear at node no. For the pinion rate $\dot{\theta}_{pe} = (v_1 - v_2)/r_{pe}$ and for $v_1 = C_{v1}v_s$ and $v_2 = C_{v2}v_s$ from the JPL–IDEAS code, one obtains

$$v_1 - v_2 = \frac{C_{soe}v_s}{r_{pe}}$$

where v_s is a modal velocity defined in Eq. (2) and $C_{soe} = C_{v1} - C_{v2}$. Therefore, $\dot{\theta}_{pe} = C_{spe}v_s = [0 \; C_{spe}]x_s$, where $C_{spe} = C_{soe}/r_{pe}$, finally giving

$$C_{s3} = [0 \; C_{spe}] \tag{6b}$$

The matrix C_{soe} is directly obtained from the JPL–IDEAS code.

The azimuth position angle is obtained as $\theta_a = C_a q_s$, where C_a is a result of the JPL–IDEAS code and, thus, $\theta_a = [C_a \; 0]x_s, \dot{\theta}_a = [0 \; C_a]x_s$. Therefore,

$$C_{s4} = [C_a \; 0], \qquad C_{s5} = [0 \; C_a] \tag{6c}$$

The last seven rows of C_s are obtained from the finite-element model. For azimuth pinion rates $\dot{\theta}_{pa1} = [0 \; C_{pa1}]x_s, \dot{\theta}_{pa2} = [0 \; C_{pa2}]x_s$, pointing errors $\epsilon_{el} = [C_{ere} \; 0]$, $\epsilon_{xel} = [C_{erx} \; 0]$, and subreflector positions $q_{sx} = [C_{sx} \; 0]$, $q_{sy} = [C_{sy} \; 0]$, and $q_{sz} = [C_{sz} \; 0]$, thus,

$$C_{s6} = [0 \; C_{pa1}], \qquad C_{s7} = [0 \; C_{pa2}] \tag{6d}$$

$$C_{s8} = [C_{ere} \; 0] \qquad C_{s9} = [C_{erx} \; 0] \tag{6e}$$

$$C_{s10} = [C_{sx} \; 0], \qquad C_{s11} = [C_{sy} \; 0], \qquad C_{s12} = [C_{sz} \; 0] \tag{6f}$$

3. Matrix B_S. The inputs to the structure are: an elevation-axis drive torque, two azimuth-axis drive torques, and a wind disturbance force. The elevation-axis drive torque is applied to the elevation bull gear by the pinion, as shown in Fig. 1. A node labeled $no = 86302$ in the finite-element model is the point of contact between the pinion and the bull gear, while a node with the label $nu = 86881$ is located at the joint between the supporting truss structure and the pinion housing. The rigid pinion housing includes two drive systems. Consider forces at nodes no and nu and their components tangential to the bull gear at node no (F_{tno}) and at node nu (F_{tnu}). Assuming a rigid pinion, the torque applied to the pinion of the gearbox is

$$T = \frac{F_{tno} - F_{tnu}}{r_{pe}}$$

where r_{pe} is the elevation pinion radius. From the JPL–IDEAS code, one obtains the relative tangential displacement Δq_{te} of nodes no and nu, in modal coordinates,

$$\Delta q_{te} = q_{tno} - q_{tnu} = C_{soe}q_s$$

where the matrix C_{soe} has been already described. Thus, the matrix B_{soe} for the force $\Delta F_{te} = F_{tno} - F_{tnu}$ is

$$B_{soe} = \frac{M_m^{-1}C_{soe}^T}{r_{pe}}$$

and the matrix B_{se} for the elevation torque is

$$B_{se} = \begin{bmatrix} 0 \\ B_{soe} \end{bmatrix} \tag{7a}$$

The matrices B_{sa1} and B_{sa2} for the azimuth-axis drive torques are obtained as follows. The tangential displacements of the azimuth pinion contact points are given by

$$q_{t1} = C_{sa1}q_s, \qquad q_{t2} = C_{sa2}q_s$$

where q_{t1} and q_{t2} are the tangential displacements, C_{sa1} and C_{sa2} are determined from the JPL–IDEAS finite-element model, and q_s is the modal displacement vector of the structure. Thus, the azimuth-axis drive input matrices are

$$B_{sa1} = \begin{bmatrix} 0 \\ M_m^{-1} C_{sa1}^T \end{bmatrix}, \qquad B_{sa2} = \begin{bmatrix} 0 \\ M_m^{-1} C_{sa2}^T \end{bmatrix} \tag{7b}$$

Wind disturbances are applied as wind forces from the x and y directions (x is the elevation axis direction and y is a horizontal direction orthogonal to the elevation axis). The input matrices B_{wx} and B_{wy} for the wind forces are obtained from the JPL–IDEAS model; hence, the wind input matrix is

$$B_{wind} = \begin{bmatrix} 0 & 0 \\ B_{wx} & B_{wy} \end{bmatrix} \tag{7c}$$

4. Matrix D_S. Matrix D_s is a zero matrix of dimensions $q \times p$, where q is the number of outputs and p is the number of inputs to the structure.

B. Model Reduction

The structural model under consideration consists of 21 modes or 42 states. However, some of these modes are insignificant and can be eliminated. Observability and controllability properties are used to determine modes for elimination. A balanced representation [2] is a state-space representation with its states equally controllable and observable, and the Hankel singular value is the measure of the joint controllability and observability of each balanced state variable. The states with small Hankel singular values can be deleted, since they are weakly excited and weakly observed at the same time, causing a small modeling error. For flexible structures with small damping and distinct poles, the modal representation is almost balanced, cf. [3,4,5]. Each mode has almost the same controllability and observability property; hence, each mode can be considered for reduction separately. For a structure with m modes, matrix B_s has $2m$ rows and matrix C_s has $2m$ columns. Denote b_s as the last m rows of B_s, c_q as the first m columns of C_s, and c_r as the last m columns of C_s, then b_{si} is the ith row of b_s, c_{qi} is the ith column of c_q, and c_{ri} is the ith column of c_r. The Hankel singular value for the ith mode is given by Eq. (53) of [4] and Eq. (14) of [5]

$$\gamma_i = \frac{\sqrt{(w_{bi} b_{si} b_{si}^T)(w_{qi} c_{qi}^T c_{qi} + w_{ri} \omega_i^2 c_{ri}^T c_{ri})}}{4\zeta_i \omega_i^2} \tag{8}$$

Care should be taken when determining Hankel singular values. Units should be consistent, otherwise some inputs or outputs receive more weight in Hankel singular value determination than necessary. Consider, for example, the azimuth encoder reading in arcseconds and the elevation encoder reading in degrees. For the same angle, the numerical reading of the azimuth encoder is 3600 larger than the elevation encoder reading; hence, the elements for the azimuth output are much larger than those for elevation. On the other hand, some variables need more attention than others: the pointing error and encoder readings are the most important factors in the antenna performance; hence, their importance has to be emphasized in mode evaluation. For these two reasons, consistency of units and variable importance, the weighting factors $w_{bi} > 0, w_{qi} > 0$, and $w_{ri} > 0$ for $i = 1, \cdots, m$ are introduced. Typically, weights are set to 1. However, for more important variables, the weight is set larger than 1.

For each mode, the Hankel singular value is determined and used to decide the number of modes in the reduced structural model. For the rigid-body modes, Hankel singular values tend to infinity; hence, rigid-body modes are always included in the reduced model. Hankel singular values, with all weights set to one, of the 19 flexible modes of the antenna model are plotted in Fig. 2.

The reduced order model consists of 10 modes: two rigid-body modes and eight elastic modes, with natural frequencies 3.1240, 3.4880, 4.1140, 4.4450, 6.5820, 7.1540, 7.4880, and 9.112 Hz (shadowed in Fig. 2). The transfer functions of the full and reduced models of the antenna are shown in Fig. 3, indicating that the reduced model represents properties of the original system. At this stage, wind disturbances are not included in the model and, therefore, are not considered in model reduction. One should note, however, that for a model with disturbances included, a different reduced model will be obtained, as shown in Section VI of this article.

III. Drive System Model

Three antenna drives, the elevation drive (ELD) and two azimuth drives (AZD1 and AZD2), are analyzed. Each of the drives has three inputs: rate command ($\dot{\theta}_{oe}$ or $\dot{\theta}_{oa}$), torque bias (v_{bse} or v_{bsa1}, v_{bsa2}), and pinion rate ($\dot{\theta}_{pe}$ or $\dot{\theta}_{pa1}, \dot{\theta}_{pa2}$), and the following outputs: torques (T_e or

T_{a1}, T_{a2}) and bias voltages (v_{c1}, v_{c2}) to balance the load between two azimuth drives. The amplification parameter k_a is given in Appendix A.

A. Full Model

The structure of each drive is the same, as shown in Fig. 4. The structure consists of two identical subsystems denoted G_o (which model the motor, amplifier, gearbox, tachometer, and rate-loop compensation electronics), the command amplifier G_c, and the torque share bias loop. The subsystem G_c is shown in Fig. 5. Denoting the first state variable $x_1 = v_1$, the G_c subsystem's state equation is

$$\dot{x}_1 = -\tau_1^{-1} x_1 + k_1 k_s \tau_1^{-1} \dot{\theta}_o \tag{9}$$

The equations for subsystem G_o are derived in [1]. The inputs are a biased rate command (v_1) and pinion rate ($\dot{\theta}_p$). An additional brake parameter κ, will be discussed later. The outputs are motor current (i_o), motor angular velocity (ω_m), and torque (T). These outputs are the fifth, sixth, and seventh states, respectively, in the following state-space equations for subsystem G_o

$$\dot{x}_o = A_o x_o + B_{11} v_1 + B_{12} \dot{\theta}, \qquad \begin{bmatrix} T \\ i_o \end{bmatrix} = C_o x_o \tag{10}$$

where

$$A_o = \begin{bmatrix} 0 & 1 & 0 & 0 & 0 & 0 & 0 \\ 0 & -\frac{1}{\tau_3} & 0 & 0 & 0 & -k_{tach} & 0 \\ 0 & 0 & 0 & 1 & 0 & 0 & 0 \\ \frac{k_r}{\tau_3} & \frac{k_r \tau_2}{\tau_3} & 0 & -\frac{1}{\tau_5} & -k_{cur} & 0 & 0 \\ 0 & 0 & \frac{k_f k_i}{L_a \tau_5} & \frac{k_f k_i \tau_4}{L_a \tau_5} & -\frac{R_a}{L_a} & -\frac{k_b}{L_a} & 0 \\ 0 & 0 & 0 & 0 & \frac{k_m}{J_m} & 0 & -\frac{1}{J_m N} \\ 0 & 0 & 0 & 0 & 0 & k_{gx} N_x & 0 \end{bmatrix}$$

$$B_{11}^T = [0\ 1\ 0\ 0\ 0\ 0\ 0],\ B_{12}^T = [0\ 0\ 0\ 0\ 0\ 0\ -k_{gx} N_x N]$$

$$C_{11} = [0\ 0\ 0\ 0\ 0\ 0\ 1],\ C_{12} = [0\ 0\ 0\ 0\ 1\ 0\ 0]$$

$$C_o = \begin{bmatrix} C_{11} \\ C_{12} \end{bmatrix}, \qquad B_o = [B_{11}\ B_{12}]$$

Two systems' G_o's are located in the drive system, see Fig. 4: the first one with inputs $v_{11}, \dot{\theta}_p$, outputs T_1, i_{o1}, and state vector x_{21}; and the second one with inputs $v_{12}, \dot{\theta}_p$, outputs T_2, i_{o2}, and state vector x_{22}. The equations for these systems are

$$\dot{x}_{21} = A_o x_{21} + B_{11} v_{11} + B_{12} \dot{\theta}, \qquad \begin{bmatrix} T_1 \\ i_{o1} \end{bmatrix} = C_o x_{21} \tag{11}$$

$$\dot{x}_{22} = A_o x_{22} + B_{11} v_{12} + B_{12} \dot{\theta}, \qquad \begin{bmatrix} T_2 \\ i_{o2} \end{bmatrix} = C_o x_{22} \tag{12}$$

The amplifier for the bias signal has an input of Δv_c and an output of v_u. Denoting $x_3 = v_u$, this amplifier's state-space equation is obtained

$$\dot{x}_3 = -\tau_6^{-1} x_3 + k_{ctfr} \tau_6^{-1} \Delta v_c \tag{13}$$

The nodal equations complete the set of the drive-system model equations

$$T = T_1 + T_2, \quad T_1 = C_{11} x_{21}, \quad T_2 = C_{11} x_{22} \tag{14a}$$

$$\begin{aligned} \Delta v_c &= v_{c1} - v_{c2} + k_{bs} v_{bias} \\ &= k_{ct} C_{12} (x_{21} - x_{22}) + k_{bs} v_{bias} \end{aligned} \tag{14b}$$

$$v_{11} = v_1 - v_u = x_1 - x_3, \qquad v_{12} = v_1 + v_u = x_1 + x_3 \tag{14c}$$

$$v_c = v_{c1} + v_{c2} = k_{ct} C_{12} (x_{12} + x_{22}) \tag{14d}$$

Denoting the state vector $x_m^T = [x_1^T, x_{21}^T, x_{22}^T, x_3^T]$ and combining Eqs. (9) through (14), one can write the equations for the drive system as follows:

$$\dot{x}_m = A_m x_m + B_m u_m, \qquad y_m = C_m x_m \tag{15}$$

where $u_m^T = [\dot{\theta}_o\ \dot{\theta}_p\ v_{bias}]$, $y_m^T = [T\ v_c\ \omega_{m1}\ \omega_{m2}]$, and

$$A_m = \begin{bmatrix} -1/\tau_1 & 0 & 0 & 0 \\ B_{11} & A_o & 0 & -B_{11} \\ B_{11} & 0 & A_o & B_{11} \\ 0 & p_1 & -p_1 & -1/\tau_6 \end{bmatrix}$$

$$B_m = [B_{mo}\ B_{mp}\ B_{mbs}] = \begin{bmatrix} k_1 k_s/\tau_1 & 0 & 0 \\ 0 & B_{12} & 0 \\ 0 & B_{12} & 0 \\ 0 & 0 & p_2 \end{bmatrix}$$

$$C_m = \begin{bmatrix} C_{mt} \\ C_{mc} \\ C_{om1} \\ C_{om2} \end{bmatrix} = \begin{bmatrix} 0 & C_{11} & C_{11} & 0 \\ 0 & k_{ct}C_{12} & k_{ct}C_{12} & 0 \\ 0 & C_{13} & 0 & 0 \\ 0 & 0 & C_{13} & 0 \end{bmatrix}$$

$$p_1 = \frac{k_{ctfr}k_{ct}C_{12}}{\tau_6}, \qquad p_2 = \frac{k_{ctfr}k_{ct}}{\tau_6}$$

$$C_{13} = [0\ 0\ 0\ 0\ 0\ 1\ 0]$$

B. Model Reduction

The drive system model is reduced by applying the balancing principle. The system has a pole at zero; hence, the grammians and Hankel singular values do not exist, but tend toward infinity. It is shown in Appendix B that the balanced representation exists for the case of poles at zero. The reduction using antigrammians can be completed. Note that the reduction of a triple (A, B, C) leads now to the quadruple (A_r, B_r, C_r, D_r). This fact has to be taken into account when deriving the rate-loop model.

The drive system has 16 state variables. The plots of the singular values of the balaneed antigrammians for the elevation and azimuth drive systems are shown in Fig. 6. The singular values of component number 5 and greater are large in comparison to the remaining components. Therefore, the reduced system consists of five state variables (one state with the pole at zero). The transfer functions of the reduced and full elevation drive systems are compared in Fig. 7 (transfer function for the azimuth drives are similar). From Fig. 7, one can see that the reduced model almost exactly approximates the full model.

IV. Rate-Loop Model

In this section a rate-loop model with active azimuth and elevation drives is presented. Also, a model with an active elevation drive and with activated azimuth brakes is derived, along with a model with an active azimuth drive and with elevation brakes activated. The obtained rate-loop models are reduced to obtain the smallest acceptable model.

A. Full Model

The rate-loop model of the antenna is shown in Fig. 8. The model consists of the antenna structure model and models of three drives: the elevation drive (ELD) and two azimuth drives (AZD1 and AZD2) described above.

Combining the equations for structure and the ELD, AZD1, and AZD2 with the nodal equations for the rate-loop model as in Fig. 10, one obtains the following equations (where the term D appeared as a result of model reduction). For the elevation drive,

$$\dot{x}_e = A_{me}x_e + [B_{moe}\ B_{mpe}\ B_{mbse}] \begin{bmatrix} \dot{\theta}_{oe} \\ \dot{\theta}_{pe} \\ v_{bse} \end{bmatrix} \tag{16a}$$

$$T_e = C_{mt}x_e + [D_{eo}\ D_{ep}\ D_{ebs}] \begin{bmatrix} \dot{\theta}_{oe} \\ \dot{\theta}_{pe} \\ v_{bse} \end{bmatrix} \tag{16b}$$

For azimuth drive AZD1,

$$\dot{x}_{a1} = A_{ma}x_{a1} + [B_{moa}\ B_{mpa1}\ B_{mbsa}] \begin{bmatrix} \dot{\theta}_{a1} \\ \dot{\theta}_{pa1} \\ v_{bsa1} \end{bmatrix} \tag{17a}$$

$$\begin{bmatrix} T_{a1} \\ v_{c1} \end{bmatrix} = \begin{bmatrix} C_{mt} \\ C_{mc} \end{bmatrix} x_{a1} + \begin{bmatrix} D_{aot} & D_{apt} & D_{abst} \\ D_{aov} & D_{apv} & D_{absv} \end{bmatrix} \begin{bmatrix} \dot{\theta}_{a1} \\ \dot{\theta}_{pa1} \\ v_{bsa1} \end{bmatrix} \tag{17b}$$

For azimuth drive AZD2,

$$\dot{x}_{a2} = A_{ma}x_{a2} + [B_{moa}\ B_{mpa2}\ B_{mbsa}] \begin{bmatrix} \dot{\theta}_{a2} \\ \dot{\theta}_{pa2} \\ v_{bsa2} \end{bmatrix} \tag{18a}$$

$$\begin{bmatrix} T_{a2} \\ v_{c2} \end{bmatrix} = \begin{bmatrix} C_{mt} \\ C_{mc} \end{bmatrix} x_{a2} + \begin{bmatrix} D_{aot} & D_{apt} & D_{abst} \\ D_{aov} & D_{apv} & D_{absv} \end{bmatrix} \begin{bmatrix} \dot{\theta}_{a2} \\ \dot{\theta}_{pa2} \\ v_{bsa2} \end{bmatrix} \tag{18b}$$

For the antenna structure,

$$y_s = C_s x_s \tag{19a}$$

$$\dot{x}_s = A_s x_s + B_{se}T_e + B_{sa1}T_{a1} + B_{sa2}T_{a2} + B_{wind}f_{wind} \tag{19b}$$

The nodal equations are

$$\dot{\theta}_{a1} = \dot{\theta}_{oa} - v_{aa} = \dot{\theta}_{oa} - k_a(v_{c1} - v_{c2}) = \dot{\theta}_{oa} - k_a C_{mc}(x_{a1} - x_{a2}) \tag{20a}$$

$$\dot{\theta}_{a2} = \dot{\theta}_{oa} + v_{aa} = \dot{\theta}_{oa} + k_a(v_{c1} - v_{c2}) = \dot{\theta}_{oa} + k_a C_{mc}(x_{a1} - x_{a2}) \tag{20b}$$

For the state vector $x_{rl}^T = [x_e^T\ x_{a1}^T\ x_{a2}^T\ x_s^T]$, the input $u_{rl} = [\dot{\theta}_{oe}\ \dot{\theta}_{oa}\ v_{bse}\ v_{bsa1}\ v_{bsa2}\ f_{wind}]^T$, the output $y_{rl} = [\theta_e\ \theta_a]^T$, and the state triple (A_{rl}, B_{rl}, C_{rl}) is found

$$A_{rl} = \begin{bmatrix} A_{me} & 0 & 0 & B_{mpe}C_{s3} \\ 0 & A_{ma} - k_a B_{moa}C_{mca} & k_a B_{moa}C_{mca} & B_{mpa}C_{s6} \\ 0 & k_a B_{moa}C_{mca} & A_{ma} - k_a B_{moa}C_{mca} & B_{mpa}C_{s7} \\ B_{se}C_{mte} & B_{sa1}C_{mta} + k_a \times (B_{sa2} - B_{sa1})D_{aot}C_{mca} & B_{sa2}C_{mta} + k_a \times (B_{sa1} - B_{sa2})D_{aot}C_{mca} & A_s + B_{se}D_{ep}C_{s3} + B_{sa1}D_{apt}C_{s6} + B_{sa2}D_{apt}C_{s7} \end{bmatrix} \tag{21a}$$

$$B_{rl} = \begin{bmatrix} B_{moe} & 0 & B_{mbse} & 0 & 0 & 0 \\ 0 & B_{moa} & 0 & B_{mbsa} & 0 & 0 \\ 0 & B_{moa} & 0 & 0 & B_{mbsa} & 0 \\ B_{se}D_{eo} & (B_{sa1} + B_{sa2})D_{aot} & B_{se}D_{ebs} & B_{sa1}D_{abst} & B_{sa2}D_{abst} & B_{wind} \end{bmatrix} \tag{21b}$$

$$C_{rl} = \begin{bmatrix} 0 & 0 & 0 & C_{s1} \\ 0 & 0 & 0 & C_{s4} \end{bmatrix} \tag{21c}$$

B. Rate-Loop Model With Active Elevation or Azimuth Brakes

Most frequently, the antenna dynamics are simulated with elevation and azimuth drives active simultaneously.

There are situations, however, when either the azimuth or elevation brakes are on and only one antenna drive is active. There are two ways of modeling the brake action in this case. In the first way, the numerical value to the parameter κ, shown in Fig. 5, is set. For an active brake, the tachometer shaft is still, hence $\omega_m = 0$. This is obtained by setting $\kappa = 0$ in Fig. 5. For the case where the brake is off, one sets $\kappa = 1$. Despite its simplicity, this approach leads to an unnecessarily large model. The dynamics of the drive with the active brakes are included in the model, although the drive is not active. This disadvantage is removed by deriving separate models for the antenna with active brakes.

Block diagrams of the antenna control systems with active brakes are shown in Fig. 9. For the active elevation brakes, the elevation torque T_e is due to elastic deformation of the pinion shaft, hence,

$$T_e = k_{goe}\theta_{pe} = k_{goe}[C_{spe}\ 0]x_s$$

Thus, the equation for the antenna structure is

$$\dot{x}_s = A_s x_s + \begin{bmatrix} 0 \\ B_{soe} \end{bmatrix} [C_{spe}\ 0]x_s + B_{sa1}T_{a1} + B_{sa2}T_{a2} \quad (22a)$$

and the following matrix for active elevation brakes is obtained:

$$A_{se} = A_s + \begin{bmatrix} 0 & 0 \\ B_{soe}C_{spe} & 0 \end{bmatrix} \quad (22b)$$

For the case of active elevation brakes, the state variable x_e representing the elevation drive is zero. These states are no longer necessary, and may be removed from the state vector x_{rl}. As a result: the first row and column of matrix A_{rl} are deleted and the matrix A_s is replaced with A_{se}; the first row and the first and third columns of matrix B_{rl} are deleted (no T_e and v_{bse} inputs); and the first column of matrix C_{rl} is removed. The block diagram of the rate-loop system with active elevation brakes is shown in Fig. 9(a).

As in the case for elevation, the torques at the azimuth drive, due to active azimuth brakes, are determined through the azimuth drive's stiffness and pinion angle of rotation

$$T_{a1} = k_{goa}\theta_{pa1} = k_{goa}[C_{spa1}\ 0]x_s$$

$$T_{a2} = k_{goa}\theta_{pa2} = k_{goa}[C_{spa2}\ 0]x_s$$

The resulting structure equation is

$$\dot{x}_s = A_s x_s + \begin{bmatrix} 0 \\ B_1 \end{bmatrix} [C_{spa1}\ 0]x_s + \begin{bmatrix} 0 \\ B_2 \end{bmatrix} [C_{spa2}\ 0]x_s + B_{se}T_e \quad (23a)$$

Thus, the structure matrix with azimuth brakes active is

$$A_{sa} = A_s + \begin{bmatrix} 0 & 0 \\ B_1C_{spa1} + B_2C_{spa2} & 0 \end{bmatrix} \quad (23b)$$

For the case where the azimuth brakes are active, the state variables x_{a1} and x_{a2}, representing the states of the azimuth drives, are zero. These states may be removed from the state vector x_{rl}. The rate-loop matrix A_{rl} in Eq. (21a) in this case has the second and the third rows and columns deleted and the matrix A_s is replaced with A_{sa}; the matrix B_{rl} has its second and third rows, and second, fourth, and fifth columns deleted (no T_{a1}, T_{a2}, and v_{bsa} inputs); and matrix C_{rl} has its second and third column deleted. The block diagram of the rate-loop system with active elevation brakes is shown in Fig. 9(b).

C. Model Reduction

Some of the poles of the rate-loop model are at zero; hence, the reduction procedure from Appendix B is applied. Note that the state triple (A_{rl}, B_{rl}, C_{rl}) is returned as a quadruple $(A_{rl}, B_{rl}, C_{rl}, D_{rl})$ after reduction

$$(A_{rl}, B_{rl}, C_{rl}) \Rightarrow (A_{rl}, B_{rl}, C_{rl}, D_{rl}) \quad (24)$$

Singular values of the balanced antigrammians of the rate-loop model are shown in Fig. 10. The rate-loop model designed from the reduced structural, elevation drive, and azimuth drive models consists of 35 states. It is reduced to 27 states—singular values of states 28 through 35 are large enough to have these states reduced. The frequency response of the reduced model is compared with the responses of the full model in Figs. 11 and 12 (the full model consists of a full antenna structural mode, and full azimuth and elevation drive models—all together 90 states).

V. Position Loop Model

The rate-loop system, with the position loop closed, is shown in Fig. 13. A proportional-plus-integral (PI) controller is applied. Consider first the series connection of the rate-loop system and the controller, as in Fig. 13(a). Define new state variables x_{ei} and x_{ai}

$$\dot{x}_{ei} = \theta_{eo} \text{ and } \dot{x}_{ai} = \theta_{ao} \tag{25}$$

and the state vector x_o for the series connection $x_o^T = [x_{rl}^T \; x_{ei} \; x_{ai}]$. The system output is

$$y_o = \begin{bmatrix} \theta_e \\ \theta_a \end{bmatrix} = \begin{bmatrix} C_e x_{rl} + d_{ee} r_e + d_{ea} r_a \\ C_a x_{rl} + d_{ae} r_e + d_{aa} r_a \end{bmatrix}$$

where d_{ee}, d_{ea}, d_{ae}, and d_{aa} are entries of D_{rl} obtained in Eq. (24). The input is $u_o^T = [\theta_{eo} \; \theta_{ao}]$ and the inputs to the rate-loop systems are

$$r_e = k_{ppe}\theta_{eo} + k_{iie}x_{ei} \text{ and } r_a = k_{ppa}\theta_{ao} + k_{iia}x_{ai} \tag{26}$$

where $k_{ppe}, k_{iie}, k_{ppa}$, and k_{iia} are proportional and integral parameters of the controllers. The equations for the rate-loop systems are

$$\dot{x}_{rl} = A_{rl}x_{rl} + B_e r_e + B_a r_a \tag{27}$$

Combining Eqs. (25), (26), and (27), one obtains

$$\dot{x}_o = A_o x_o + B_o u_o \text{ and } y_o = C_o x_o + D_o u_o \tag{28}$$

where

$$A_o = \begin{bmatrix} A_{rl} & k_{iie}B_e & k_{iia}B_a \\ 0 & 0 & 0 \\ 0 & 0 & 0 \end{bmatrix}$$

$$B_o = \begin{bmatrix} k_{ppe}B_e & k_{ppa}B_a \\ 1 & 0 \\ 0 & 1 \end{bmatrix}$$

$$C_o = \begin{bmatrix} C_e & k_{iie}d_{ee} & k_{iia}d_{ea} \\ C_a & k_{iie}d_{ae} & k_{iia}d_{aa} \end{bmatrix}$$

$$D_o = \begin{bmatrix} k_{ppe}d_{ee} & k_{ppa}d_{ea} \\ k_{ppe}d_{ae} & k_{ppa}d_{aa} \end{bmatrix}$$

and B_e and B_a are the first and the second columns of B_{rl}.

For the closed-loop system

$$u_o = y_{com} - y_o \tag{29}$$

where $y_{com}^T = [\theta_{ecom} \; \theta_{acom}]$ is a command signal. Introducing Eq. (29) to Eq. (28), one obtains

$$\left.\begin{aligned} \dot{x}_{cl} &= A_{cl}x_{cl} + B_{cl}y_{com} + B_{clw}f_w \\ y_o &= C_{cl}x_{cl} + D_{cl}y_{com} \end{aligned}\right\} \tag{30}$$

The closed-loop system matrices are

$$\left.\begin{aligned} A_{cl} &= A_o - B_oC_o, \quad B_{cl} = B_o, \\ C_{cl} &= C_o - D_oC_o, \quad D_{cl} = D_o \end{aligned}\right\} \tag{31}$$

and the wind input matrix B_{clw} is obtained from the sixth (B_{r16}) and the seventh (B_{r17}) columns of B_{rl}

$$B_{clw} = \begin{bmatrix} B_{r16} & B_{r17} \\ 0 & 0 \\ 0 & 0 \end{bmatrix}$$

The closed-loop system performance is illustrated in Figs. 14 and 15 in the frequency domain, and in Figs. 16 and 17 in the time domain.

VI. Wind Disturbance Simulations

In order to evaluate the antenna pointing error due to wind disturbances, two separate problems need to be investigated. First, wind forces acting on the antenna structure should be determined. Wind properties have been studied in [6,7], although wind forces acting on the antenna structure are not yet satisfactorily known. Secondly, the antenna model for simulation of the pointing error due to

wind disturbances should be developed. In this section, the latter problem is considered, presenting the wind disturbance simulation tools and simulation results for the assumed wind force properties.

The wind input to the antenna model is applied through the input matrix B_{wind} given in Section II. The entries of this matrix are large in comparison to the entries of the remaining input matrices B_{se}, B_{sa1}, and B_{sa2} for the elevation and azimuth pinion torques. The large values of B_{wind} appeared since the wind acts directly on the tipping structures, while torques act indirectly through the gearboxes, being reduced by the gearbox ratios. The large value of B_{wind} is a dominant factor in the reduction of the structural model; hence, it is compensated for by setting the appropriate weighting for the wind input—in this case the wind input weight is 10^{-8}. The input matrix B_{wind} is determined for a wind speed of 100 mph, and for this speed a unit wind force of $F_{ow} = 1$ lb is applied. The force F_w (lb) for the speed v_w (mph) is

$$F_w = \alpha_w^2 F_{ow} \text{ and } \alpha_w = \frac{v_w}{100} \tag{32}$$

The reduction procedure for the model with wind disturbances is similar to that presented above, however, the results are different. The plot of the Hankel singular values for the structure with the wind input is presented in Fig. 18. Comparing this plot with the one in Fig. 2 shows that a different set of modes plays the most important role in the system reduction. The wind input to the rate-loop model and the position loop model is given in Sections IV and V, respectively. The magnitude of the transfer function from the wind in the x and y directions to the elevation and cross-elevation pointing errors is shown in Fig. 19. The figures show that the flexible part of the antenna has a significant part in the pointing error balance.

Two kinds of antenna pointing error due to wind disturbances have been simulated: static error due to constant wind pressure, and dynamic error due to wind turbulence. The following results for the static wind load are obtained. For a 30-mph x-direction wind, the elevation pointing error is 2.1 mdeg and the cross-elevation pointing error is 8.9 mdeg. For a 30-mph y-direction wind, the elevation pointing error is 0.5 mdeg and the cross-elevation pointing error is 0.08 mdeg. The small pointing error due to the wind in the y direction is a result of the integrating action of the controller.

The dynamic wind force is generated as a random white-noise process pre-filtered by a filter with the spectral properties presented in Fig. 20. The obtained spectrum is an arbitrarily selected wind spectrum, a rough approximation of the Davenport model of the wind for a filter with $f_{max} = 0.1$ Hz, where f_{max} is the frequency of maximal value of the spectrum. Simulations have been performed for the position loop model consisting of 39 states. The forcing function is shown in Fig. 21, with a root mean square (rms) value equal to 0.018 lb (20 percent of the static pressure). The antenna pointing errors, in both elevation and cross-elevation, are presented in Fig. 22. For an x-direction wind, the rms error in elevation is 0.61 mdeg, and in cross-elevation it is 2.45 mdeg. For a y-direction wind, the rms error in elevation is 2.87 mdeg, while in cross-elevation, it is 0.21 mdeg. Note that the static pointing error is dominant for the x-direction wind, and the dynamic pointing error is dominant for the y-direction wind. The y-direction static action of the wind is sensed by the elevation encoder and is compensated for by the PI controller, while the static x-direction wind and the dynamic wind are barely registered by the encoder and are thus not compensated for by the controller. Again, the dynamic pointing error, due to some arbitrariness in selecting the filter, is an approximate result. More studies on wind force properties need to be done.

VII. Conclusions

In this article the modeling procedures and reduction techniques for the DSS 13 antenna structure and its control system have been presented. Through balancing the system controllability and observability properties, a reduced system model has been obtained. Antenna dynamics, rate-loop dynamics, and dynamics of a system with a closed position loop have been simulated. The model allows one to simulate elevation dynamics, cross-coupled dynamics in azimuth and elevation, and the dynamic radio-frequency pointing error due to command inputs and wind disturbances.

Acknowledgments

The authors would like to thank Robert Hill, Roy Levy, Ben Parvin, and Douglas Strain for their extensive and useful discussions.

References

[1] W. Gawronski and J. A. Mellstrom, "Elevation Control System Model for the DSS 13 Antenna," *TDA Progress Report 42-105*, vol. January–March 1991, Jet Propulsion Laboratory, Pasadena, California, pp. 82–107, May 15, 1991.

[2] B. C. Moore, "Principal Component Analysis in Linear Systems: Controllability, Observability and Model Reduction," *IEEE Transactions Autom. Control*, vol. 26, no. 1, pp. 17–32, January 1981.

[3] E. A. Jonckheere, "Principal Component Analysis of Flexible Systems—Open Loop Case," *IEEE Transactions Autom. Control*, vol. 27, no. 12, pp. 1095–1097, December 1984.

[4] W. Gawronski and J.-N. Juang, "Model Reduction for Flexible Structures," in *Control and Dynamics Systems*, edited by C. T. Leondes, vol. 36, pp. 143–222, New York: Academic Press, 1990.

[5] W. Gawronski and T. Williams, "Model Reduction for Flexible Space Structures," *Journal of Guidance, Control, and Dynamics*, vol. 14, no. 1, pp. 68–76, January 1991.

[6] R. Levy and H. McGinnes, *Wind Power Prediction Models,* NASA Technical Memorandum 33-802, NASA, Washington, D.C., November 15, 1976.

[7] M. Berg, R. Levy, H. McGinnes, and D. Strain, *Wind Speed Statistics for Goldstone, California, Anemometer Sites*, JPL Publication 81-17, Jet Propulsion Laboratory, Pasadena, California, April 15, 1981.

[8] L. Fortuna, A. Gallo, and G. Nunnar, "New Results Involving Open-Loop Balanced Realization Schemes," *Proceedings of the 28th IEEE Conference on Decision and Control*, Tampa, Florida, pp. 1331–1333, December 1989.

[9] S. Weiland, "Balanced Representations and Approximations of Linear Systems," *Proceedings of the 28th IEEE Conference on Decision and Control*, Tampa, Florida, pp. 1334–1336, December 1989.

[10] C. S. Hsu and D. Hou, *Model Reduction of Unstable Linear Control Systems*, paper presented at the Third International Conference on Advances in Communication and Control Systems, Victoria, British Columbia, Canada, 1991.

[11] R. C. Dorf, *Modern Control Systems*, Reading, Massachusetts: Addison-Wesley, 1980.

[12] R. A. Horn and C. A. Johnson, *Matrix Analysis*, Cambridge, England: Cambridge University Press, 1985.

[13] Y. Liu and B. D. O. Anderson, "Singular Perturbation Approximation of Balanced Systems," *Proceedings of the 28th IEEE Conference on Decision and Control*, Tampa, Florida, pp. 1355–1360, 1989.

[14] R. Prakash and S. Vittal Rao, "Model Reduction by Low Frequency Approximation of Internally Balanced Representation," *Proceedings of the 28th IEEE Conference on Decision and Control*, Tampa, Florida, pp. 2425–2430, 1989.

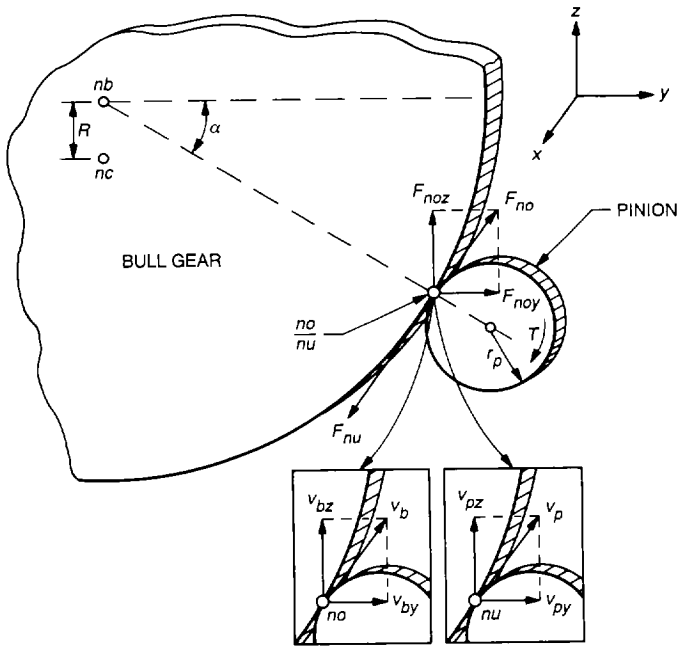

Fig. 1. Forces and velocities at the bull-gear–pinion connection.

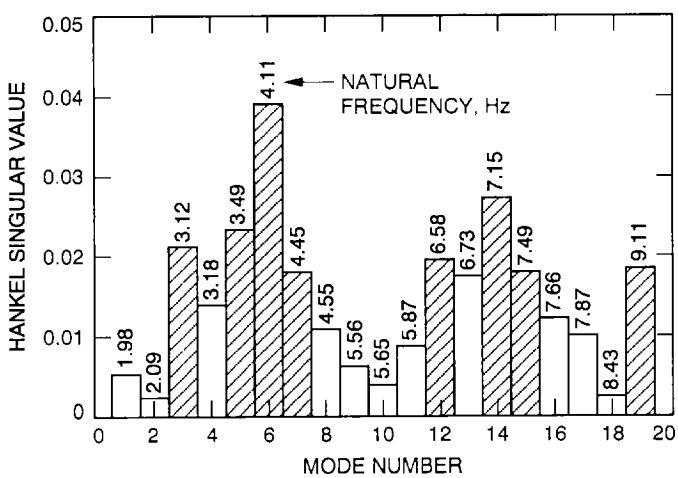

Fig. 2. Hankel singular values for the antenna structure.

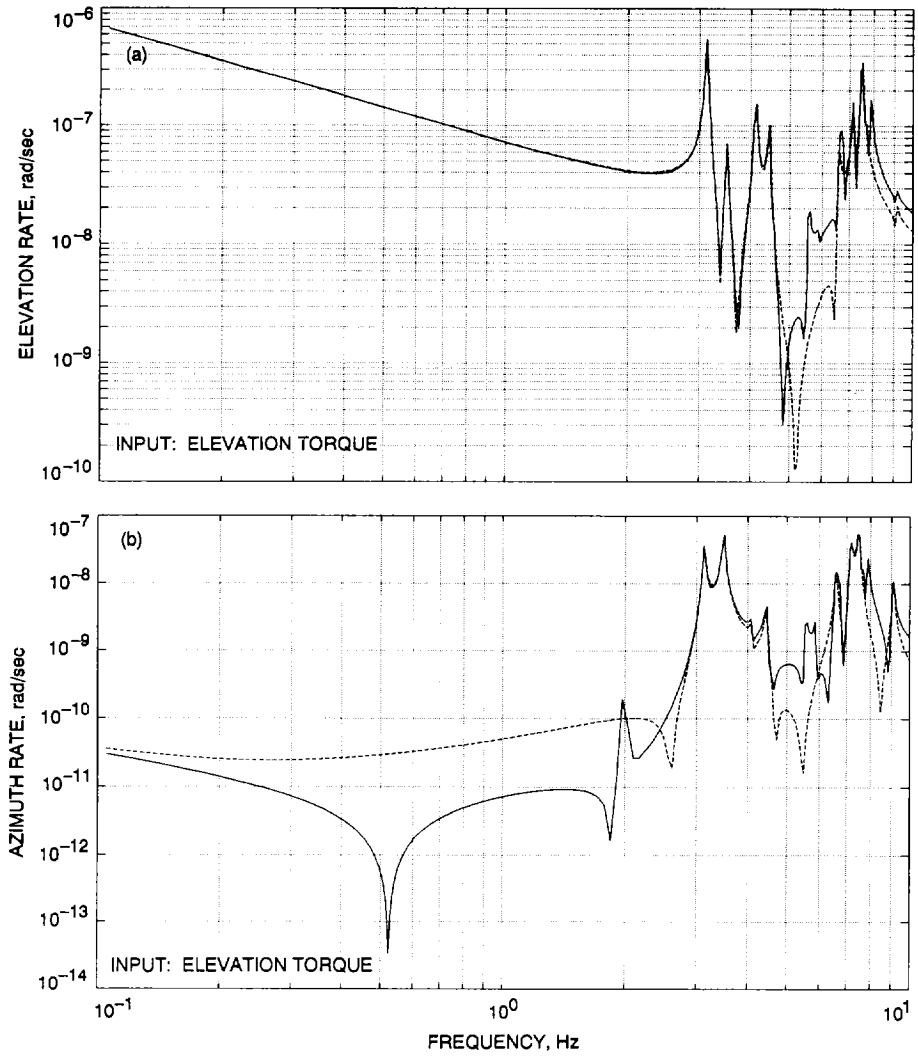

Fig. 3. Magnitudes of the transfer function of the full (42 states) (solid line) and the reduced (20 states) (dashed line) models of the antenna structure.

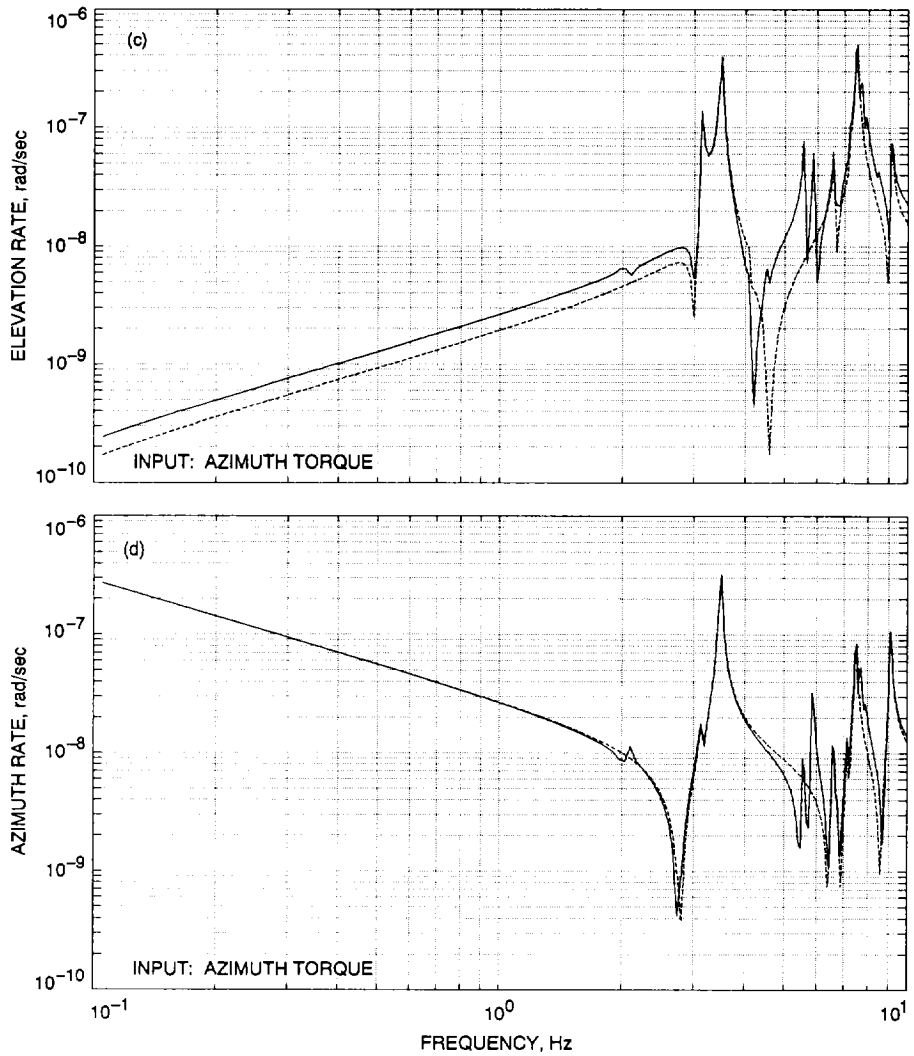
(c)
ELEVATION RATE, rad/sec
10^{-6}
10^{-7}
10^{-8}
10^{-9}
10^{-10}
INPUT: AZIMUTH TORQUE
(d)
AZIMUTH RATE, rad/sec
10^{-6}
10^{-7}
10^{-8}
10^{-9}
10^{-10}
INPUT: AZIMUTH TORQUE
10^{-1}
10^{0}
10^{1}
FREQUENCY, Hz

Fig. 3 (contd).

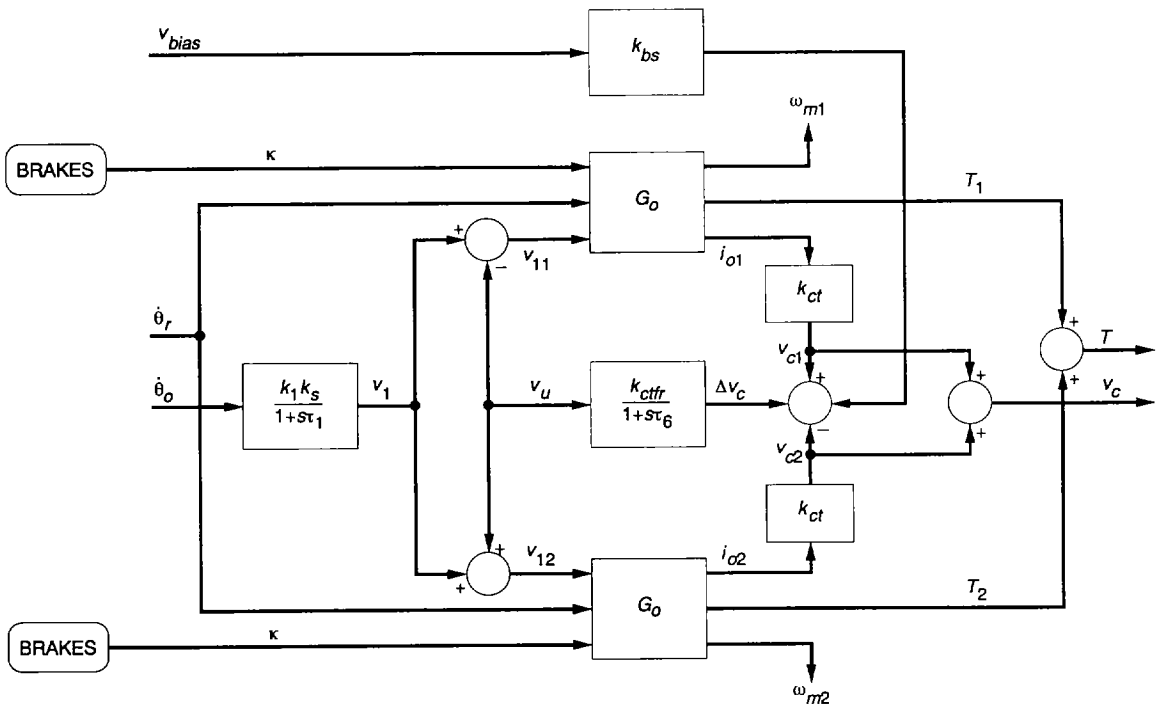

Fig. 4. Drive system model.

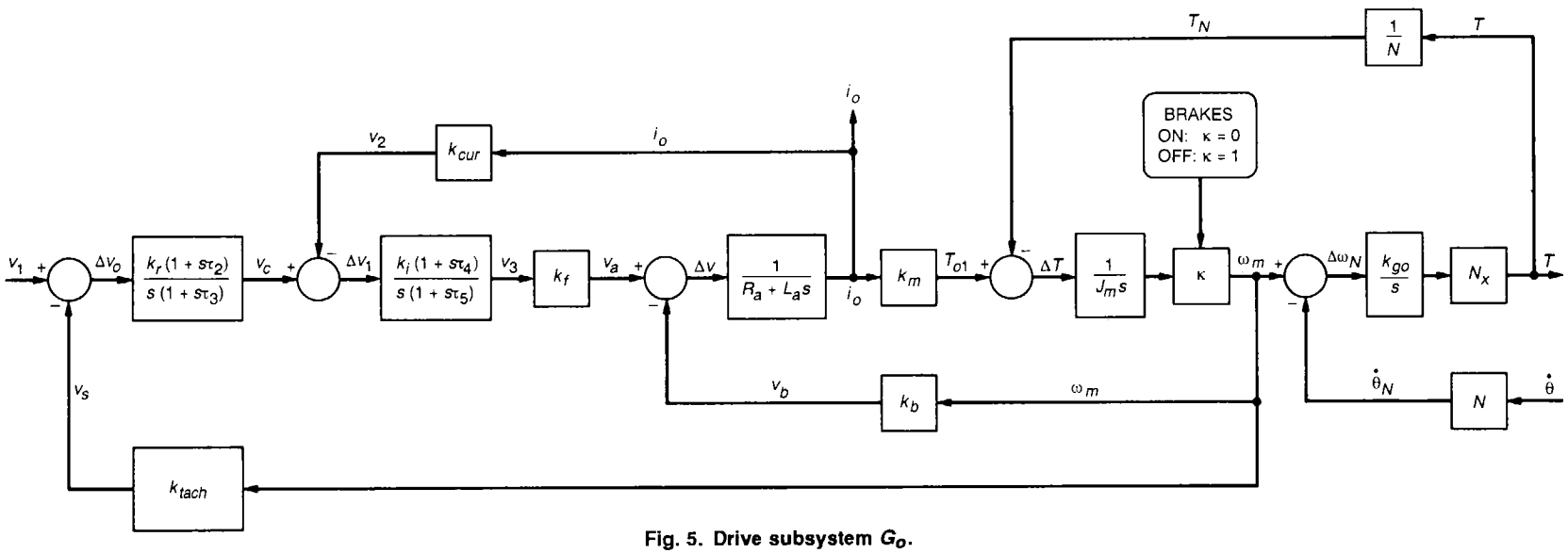

Fig. 5. Drive subsystem G_o.

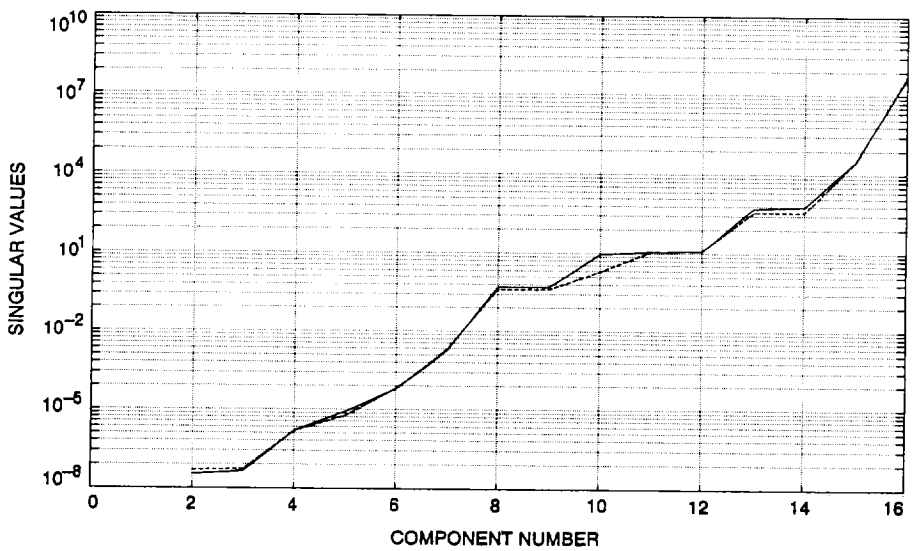

Fig. 6. Singular values of the balanced antigrammians for the elevation and azimuth drives.

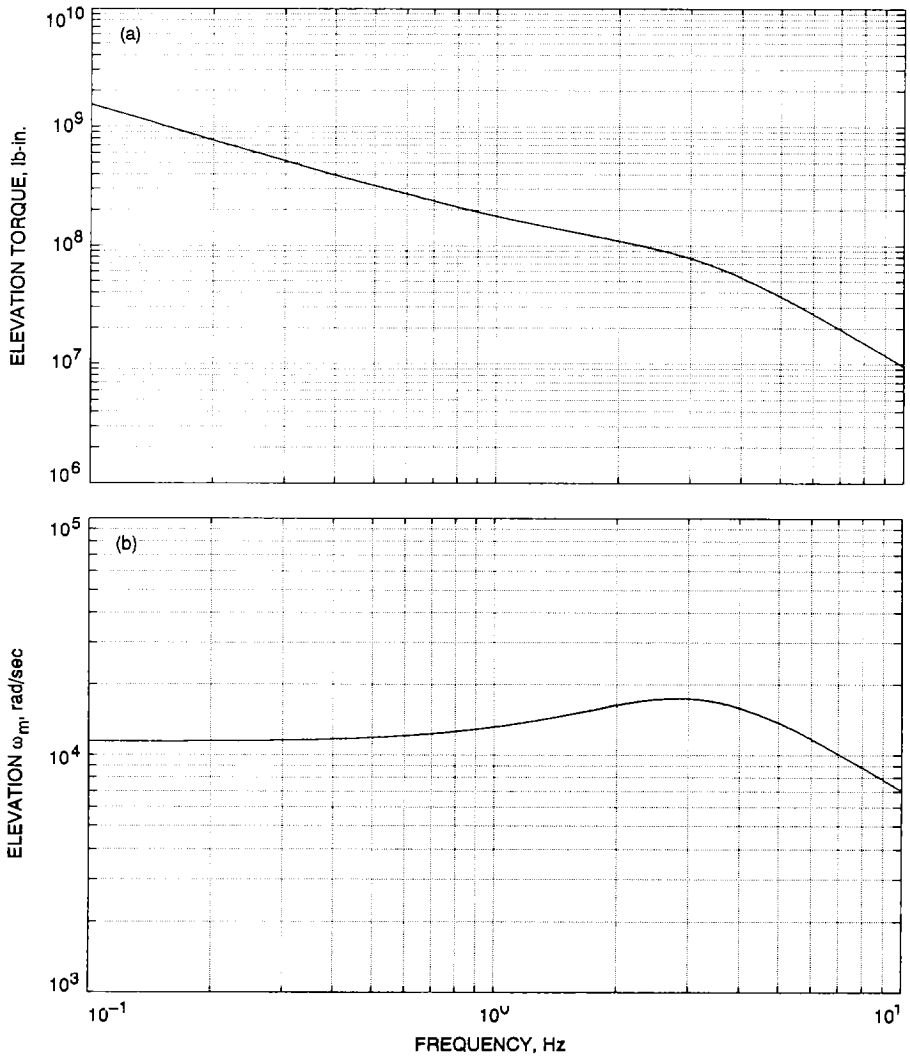

Fig. 7. Magnitudes of the transfer function of the full (16 states) and reduced (5 states) drive systems for the elevation drive input: rate command.

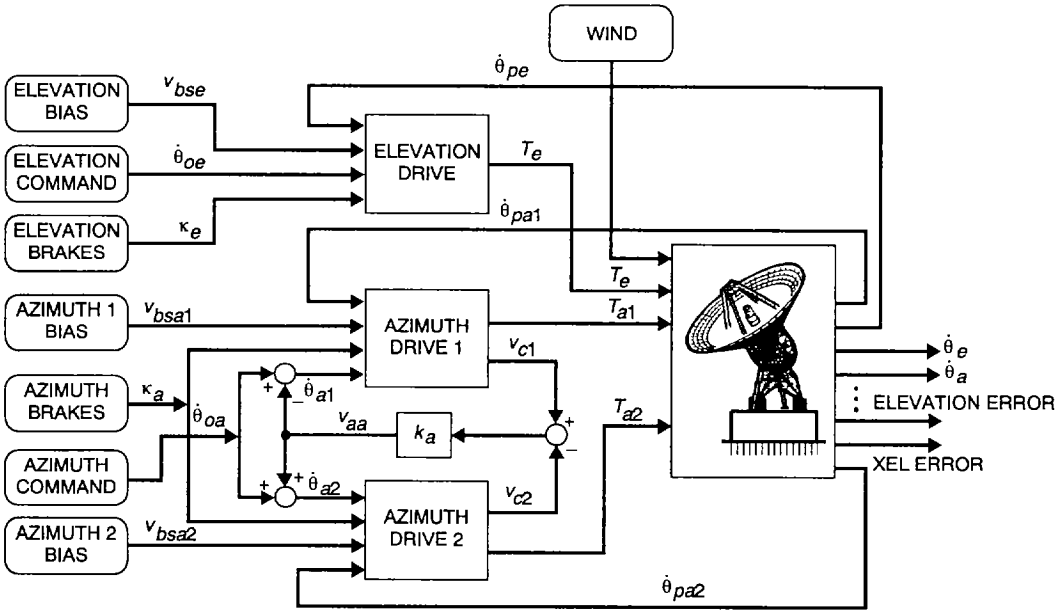

Fig. 8. Rate-loop model.

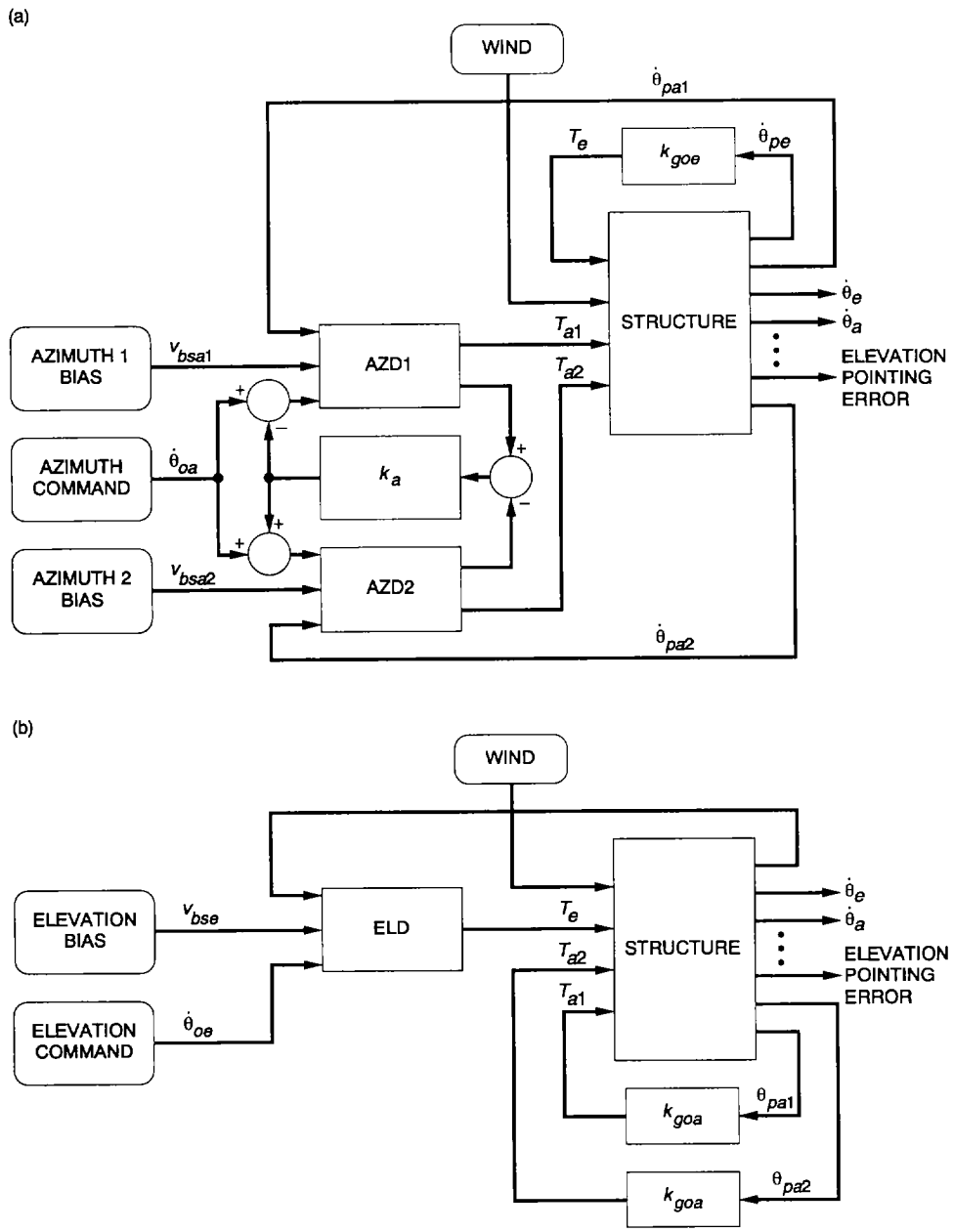

Fig. 9. Rate-loop model with active (a) elevation brakes and (b) azimuth brakes.

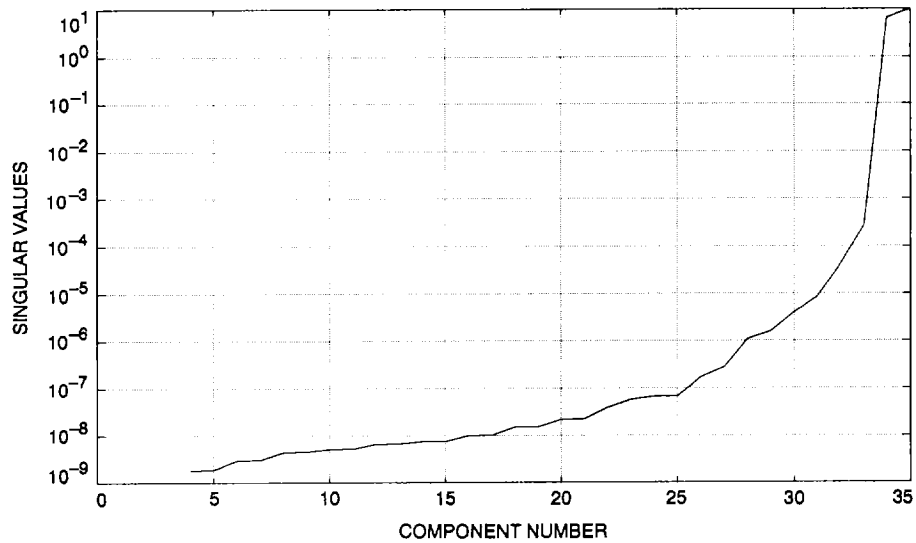

Fig. 10. Singular values of the balanced antigrammians for the rate-loop model.

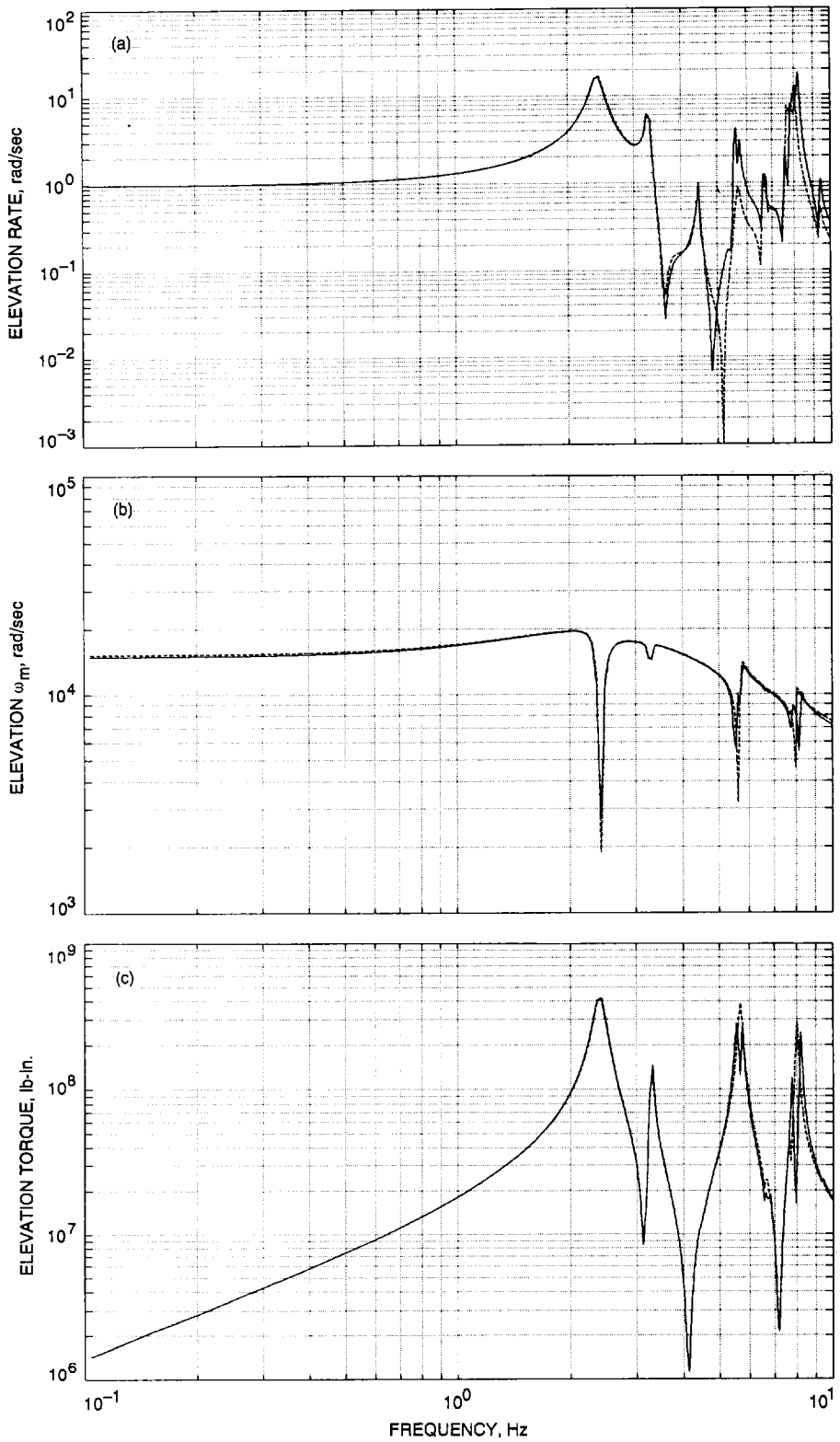

Fig. 11. Magnitudes of transfer function for the full (90 states) and the reduced (27 states) rate-loop model with elevation rate command input: (a) elevation rate, (b) elevation motor rate ω_m, (c) elevation torque, (d) azimuth rate, (e) AZ1 motor rate ω_m , and (f) AZ1 torque.

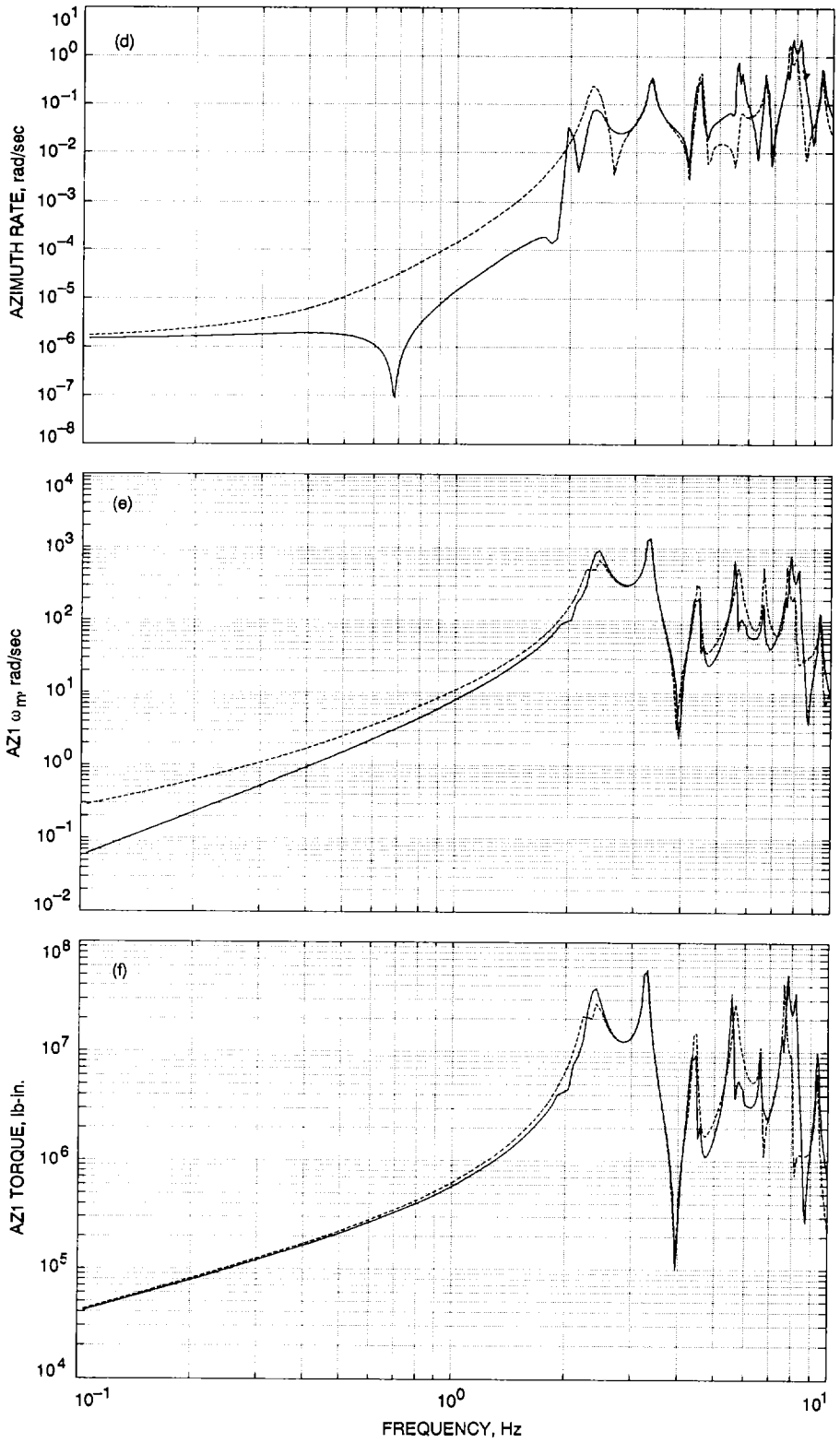
(d)
AZIMUTH RATE, rad/sec
(e)
AZ1 ωm, rad/sec
(f)
AZ1 TORQUE, lb-in.
FREQUENCY, Hz

Fig. 11 (contd).

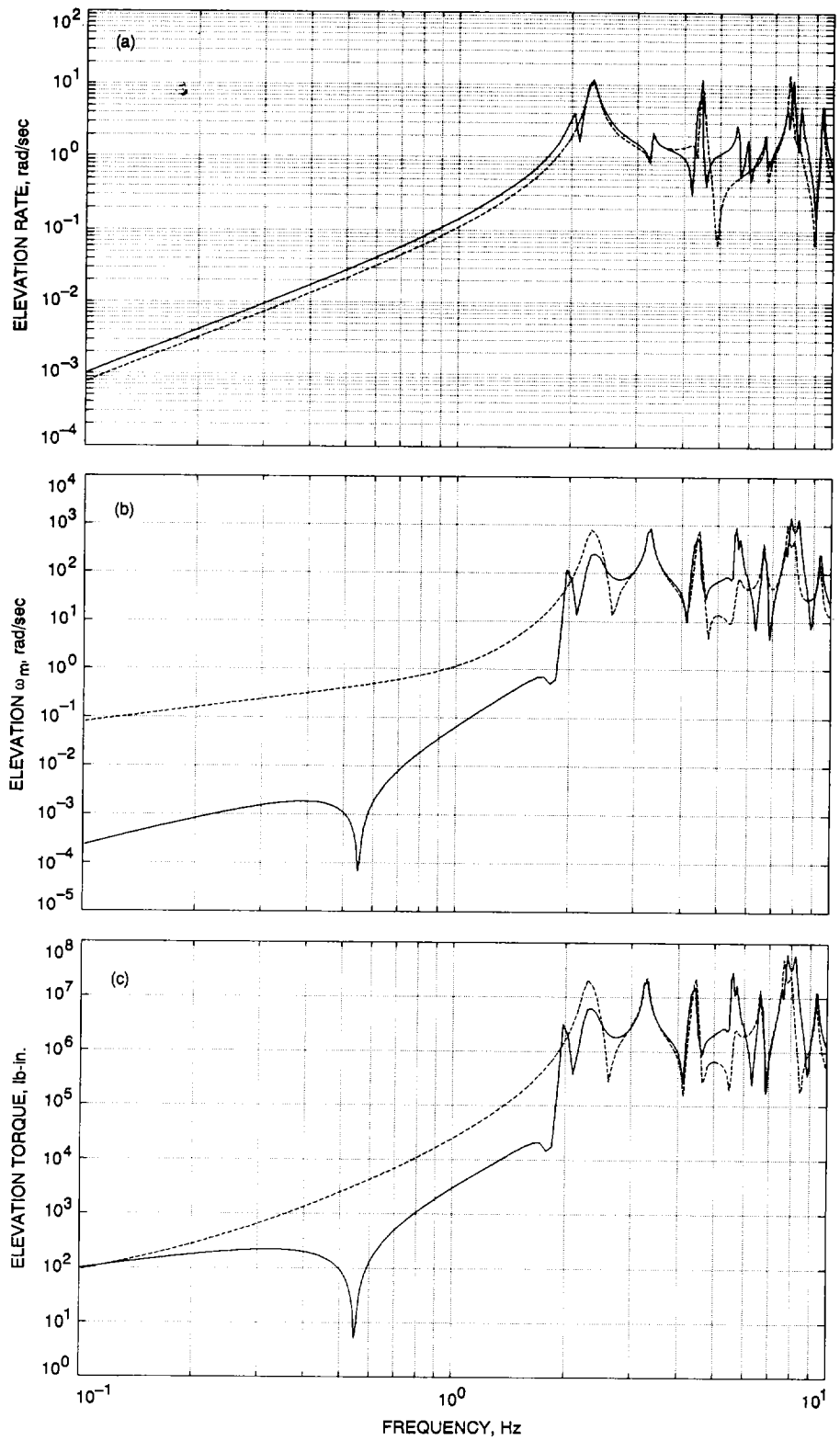

Fig. 12. Magnitudes of transfer function for the full (90 states) and the reduced (27 states) rate-loop model with azimuth rate command input: (a) elevation rate, (b) elevation motor rate ω_m , (c) elevation torque, (d) azimuth rate, (e) AZ1 motor rate ω_m , and (f) AZ1 torque.

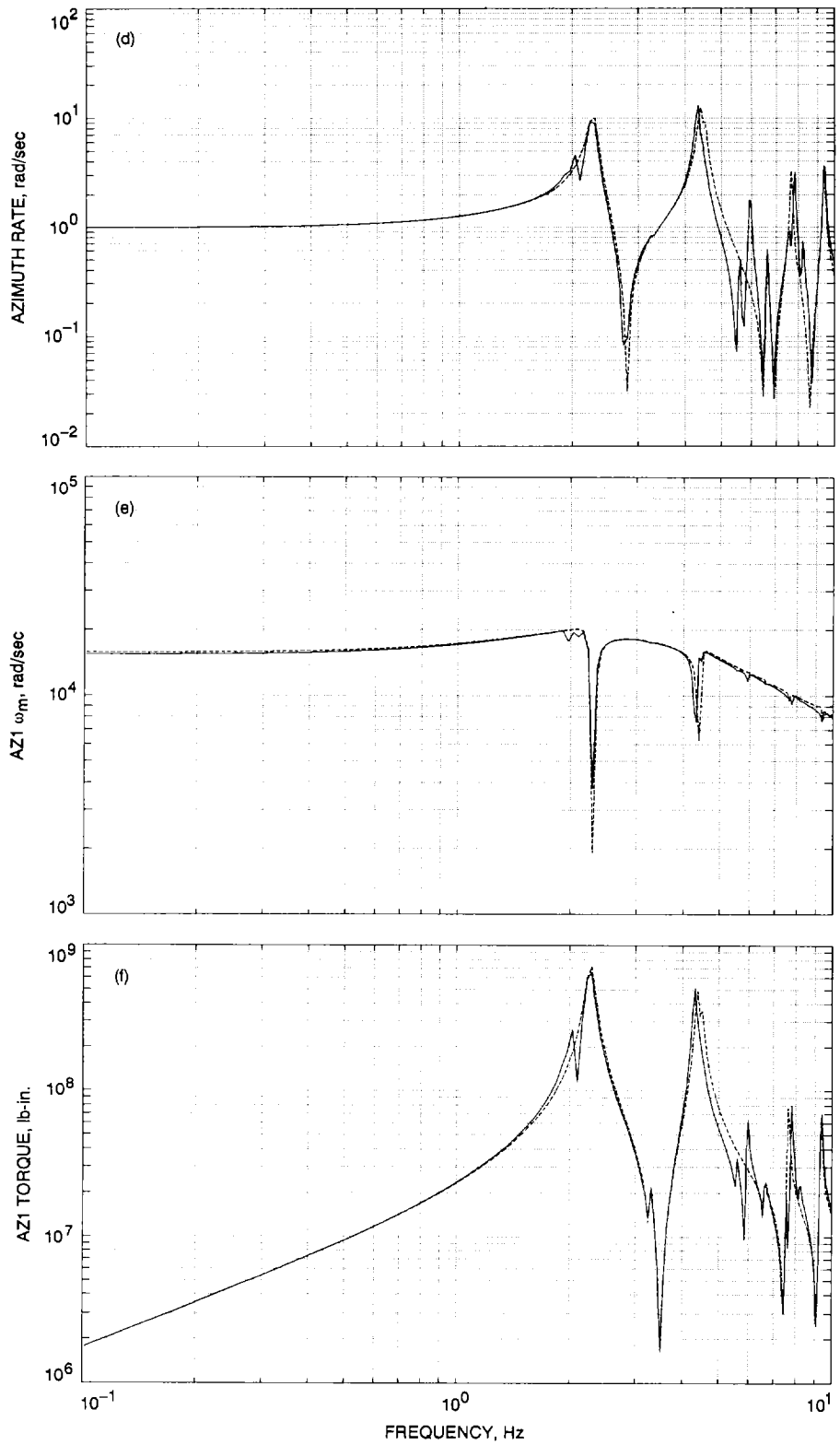
(d)
AZIMUTH RATE, rad/sec
10^2
10^1
10^0
10^{-1}
10^{-2}
(e)
AZ1 ω_m, rad/sec
10^5
10^4
10^3
(f)
AZ1 TORQUE, lb-in.
10^9
10^8
10^7
10^6
10^{-1}
10^0
10^1
FREQUENCY, Hz

Fig. 12 (contd).

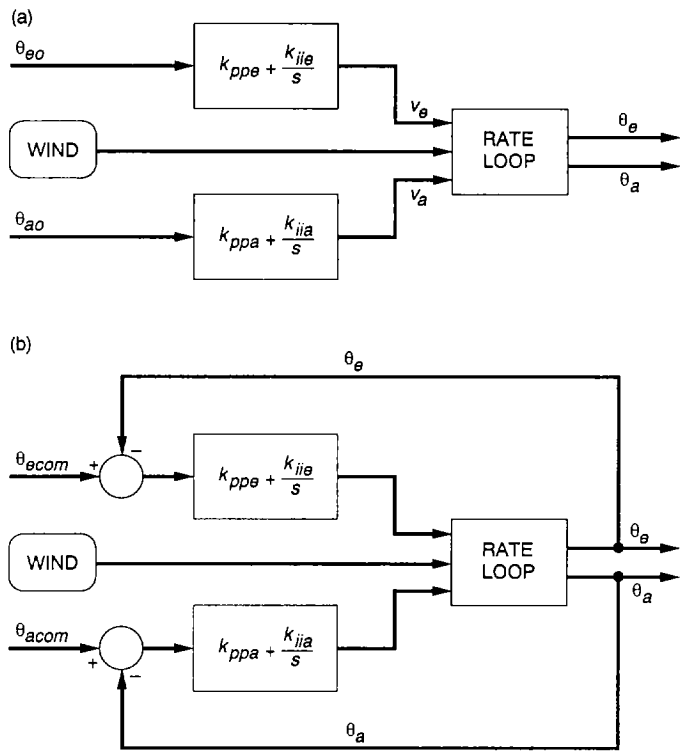

Fig. 13. Position loop system: (a) open and (b) closed.

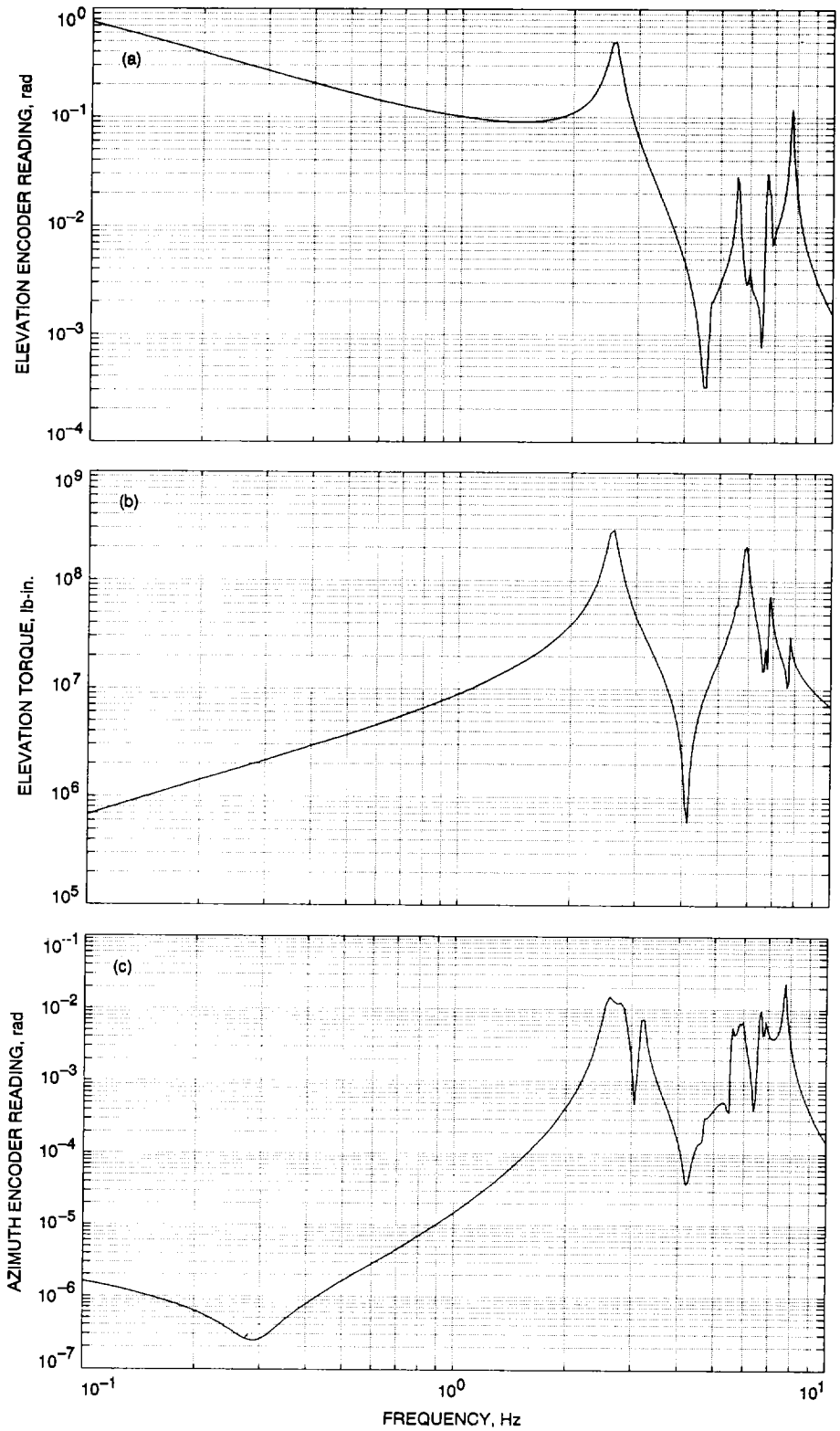

Fig. 14. Magnitudes of transfer function for the position loop system with elevation command: (a) elevation encoder reading, (b) elevation torque, (c) azimuth encoder reading, (d) AZ1 torque, (e) elevation pointing error, and (f) XEL pointing error.

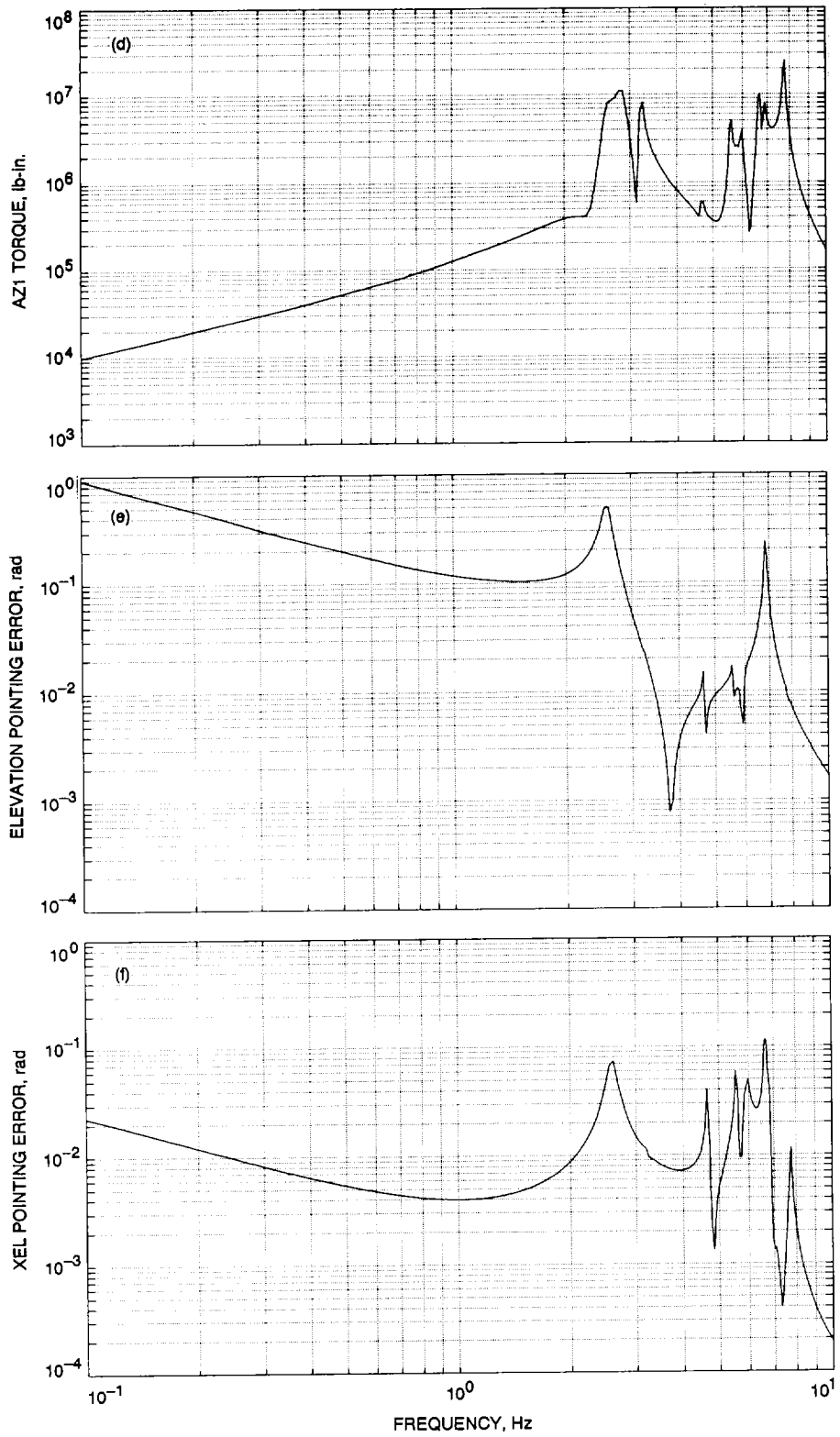
(d)
AZ1 TORQUE, lb-in.
10^8
10^7
10^6
10^5
10^4
10^3
(e)
ELEVATION POINTING ERROR, rad
10^0
10^{-1}
10^{-2}
10^{-3}
10^{-4}
(f)
XEL POINTING ERROR, rad
10^0
10^{-1}
10^{-2}
10^{-3}
10^{-4}
10^{-1}
10^0
10^1
FREQUENCY, Hz

Fig. 14 (contd).

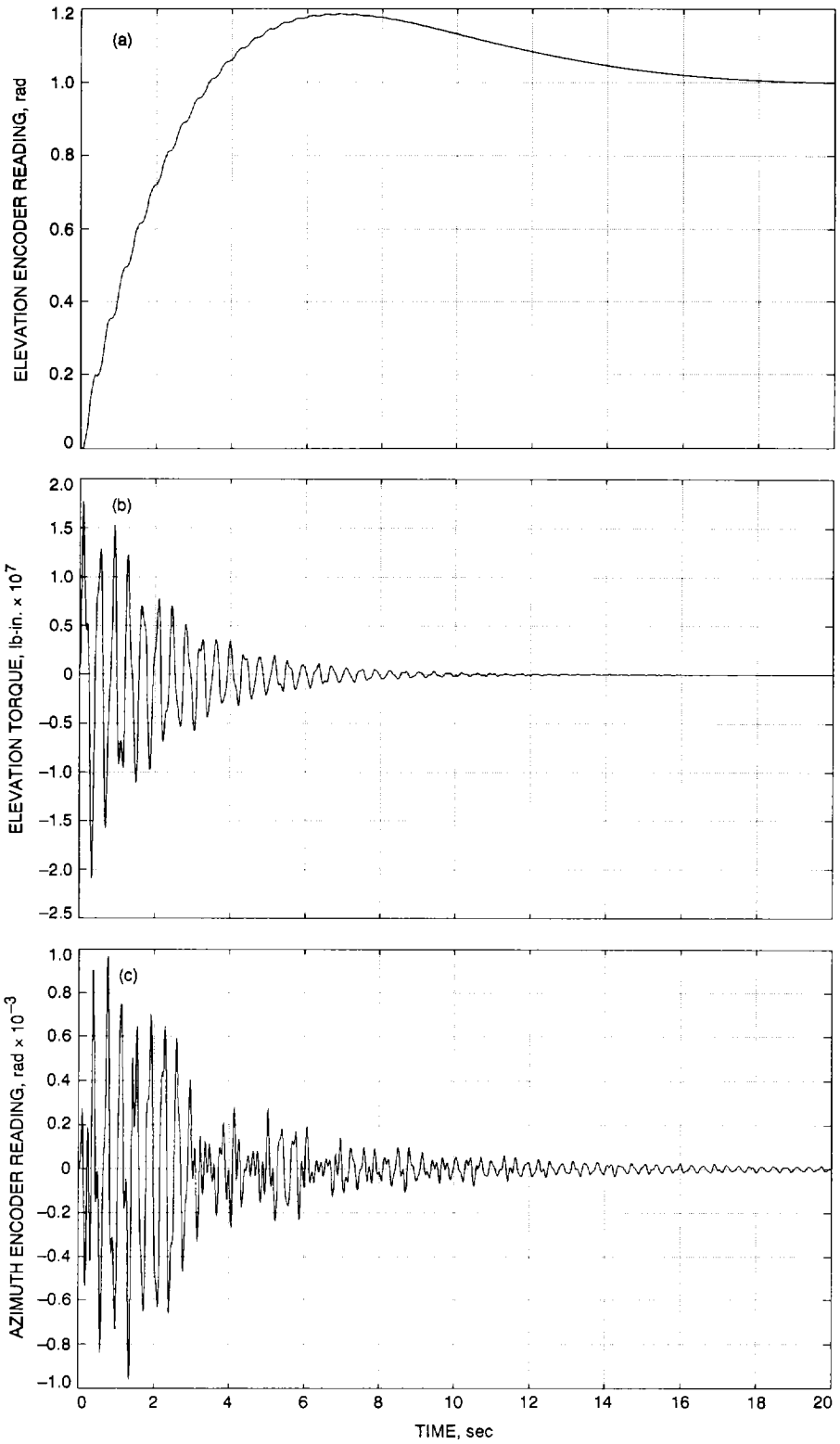

Fig. 15. Step responses of the position loop system with elevation command at 1 radian: (a) elevation encoder reading, (b) elevation torque, (c) azimuth encoder reading, (d) AZ1 torque, (e) elevation pointing error, and (f) XEL pointing error.

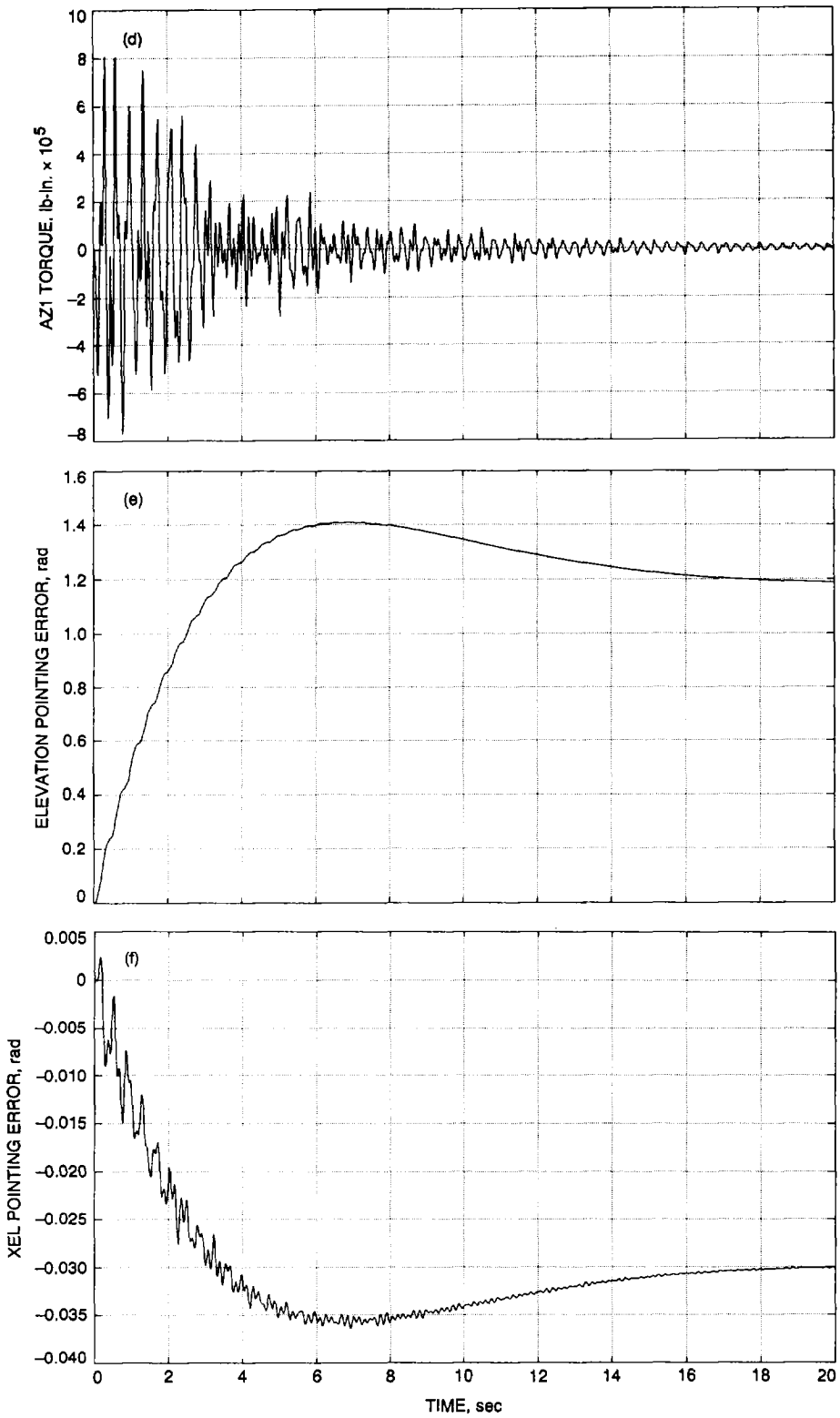
(d)
AZ1 TORQUE, lb-in. × 10^5
10
8
6
4
2
0
−2
−4
−6
−8
(e)
ELEVATION POINTING ERROR, rad
1.6
1.4
1.2
1.0
0.8
0.6
0.4
0.2
0
(f)
XEL POINTING ERROR, rad
0.005
0
−0.005
−0.010
−0.015
−0.020
−0.025
−0.030
−0.035
−0.040
0
2
4
6
8
10
12
14
16
18
20
TIME, sec

Fig. 15 (contd).

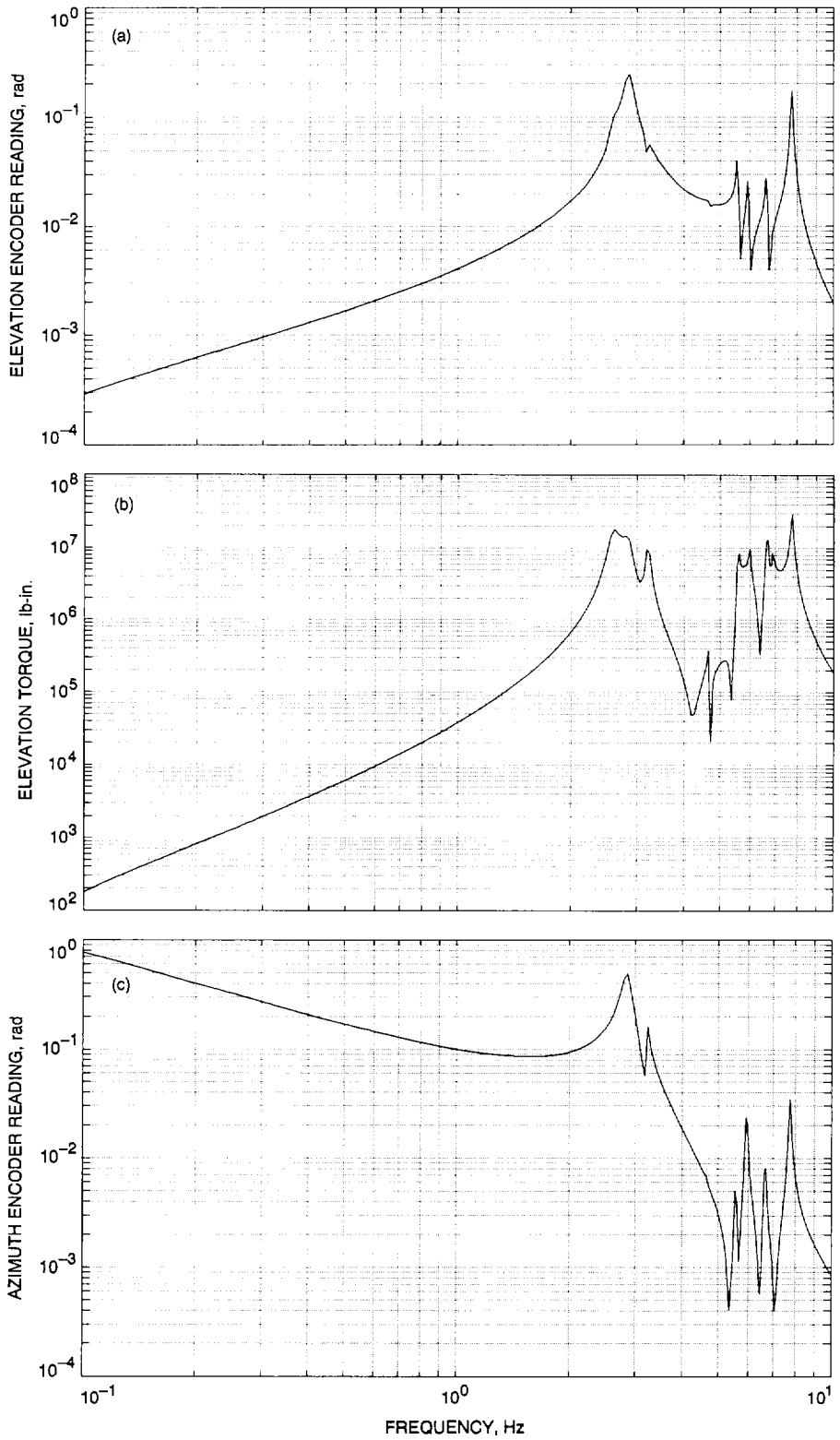

Fig. 16. Magnitudes of transfer function for the position loop system with azimuth command: (a) elevation encoder reading, (b) elevation torque, (c) azimuth encoder reading, (d) AZ1 torque, (e) elevation pointing error, and (f) XEL pointing error.

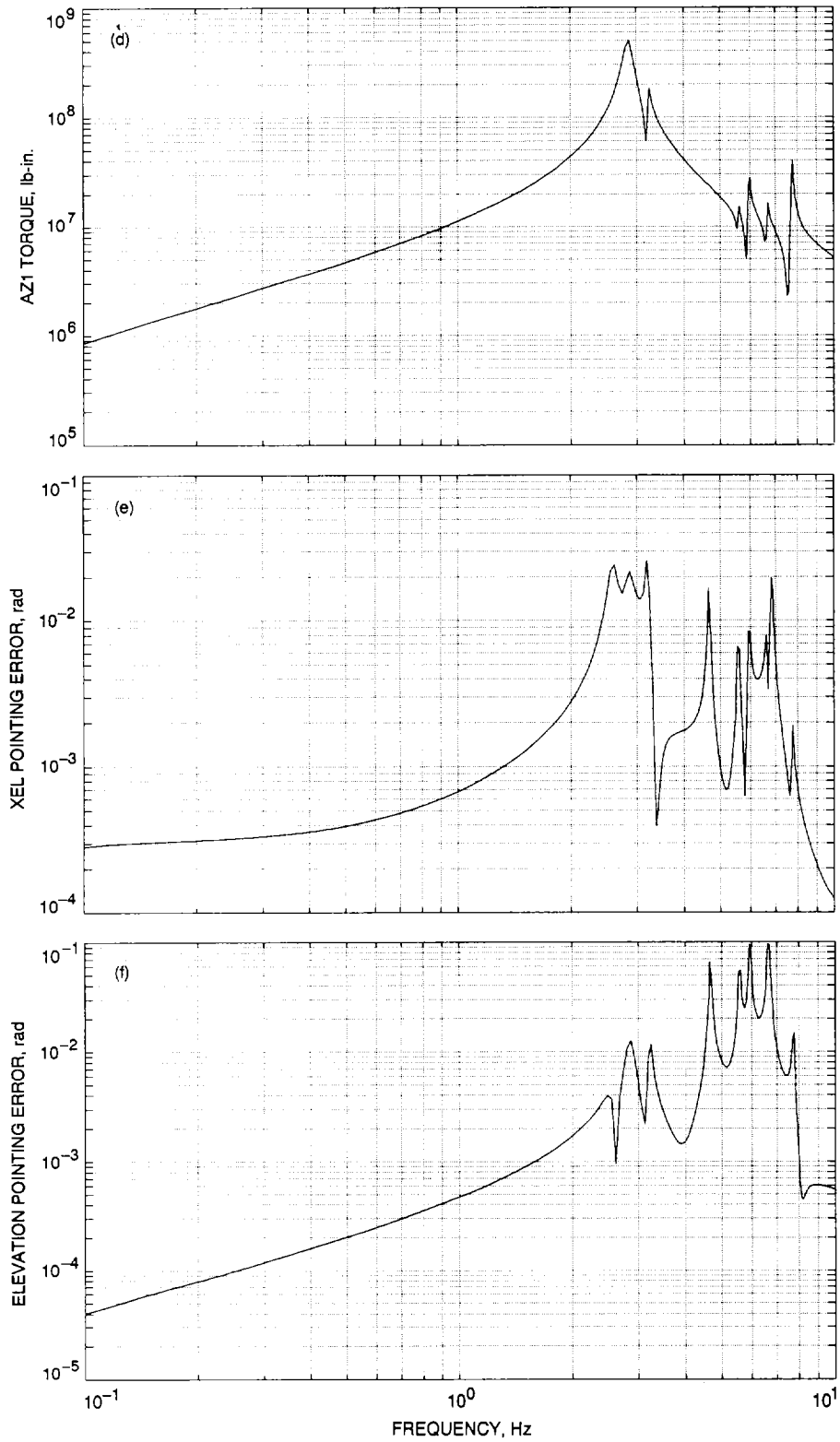
(d)
AZ1 TORQUE, lb-in.
10^9
10^8
10^7
10^6
10^5
(e)
XEL POINTING ERROR, rad
10^{-1}
10^{-2}
10^{-3}
10^{-4}
(f)
ELEVATION POINTING ERROR, rad
10^{-1}
10^{-2}
10^{-3}
10^{-4}
10^{-5}
10^{-1}
10^{0}
10^{1}
FREQUENCY, Hz

Fig. 16 (contd).

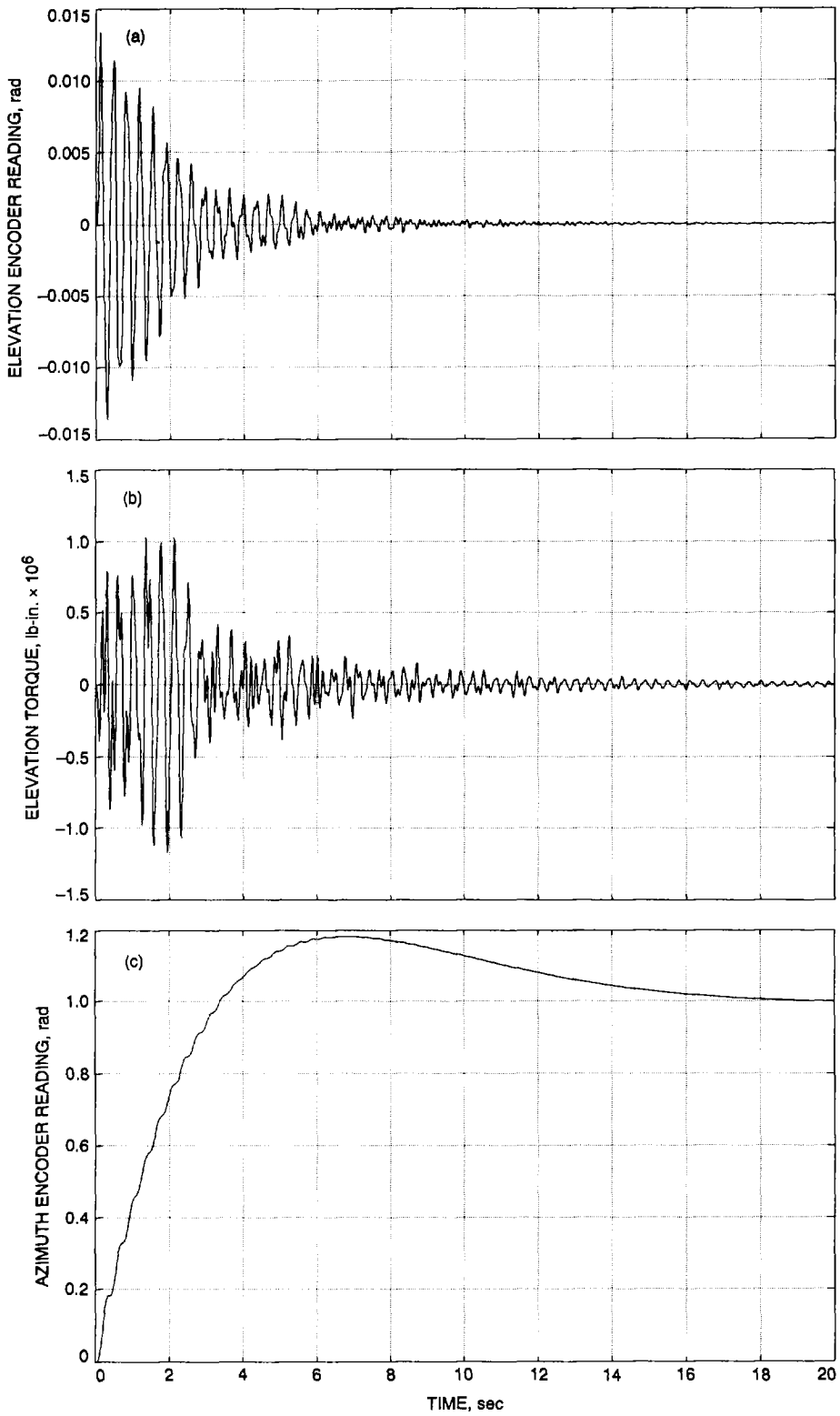

Fig. 17. Step responses of the position loop system with azimuth command at 1 radian: (a) elevation encoder reading, (b) elevation torque, (c) azimuth encoder reading, (d) AZ1 torque, (e) elevation pointing error, and (f) XEL pointing error.

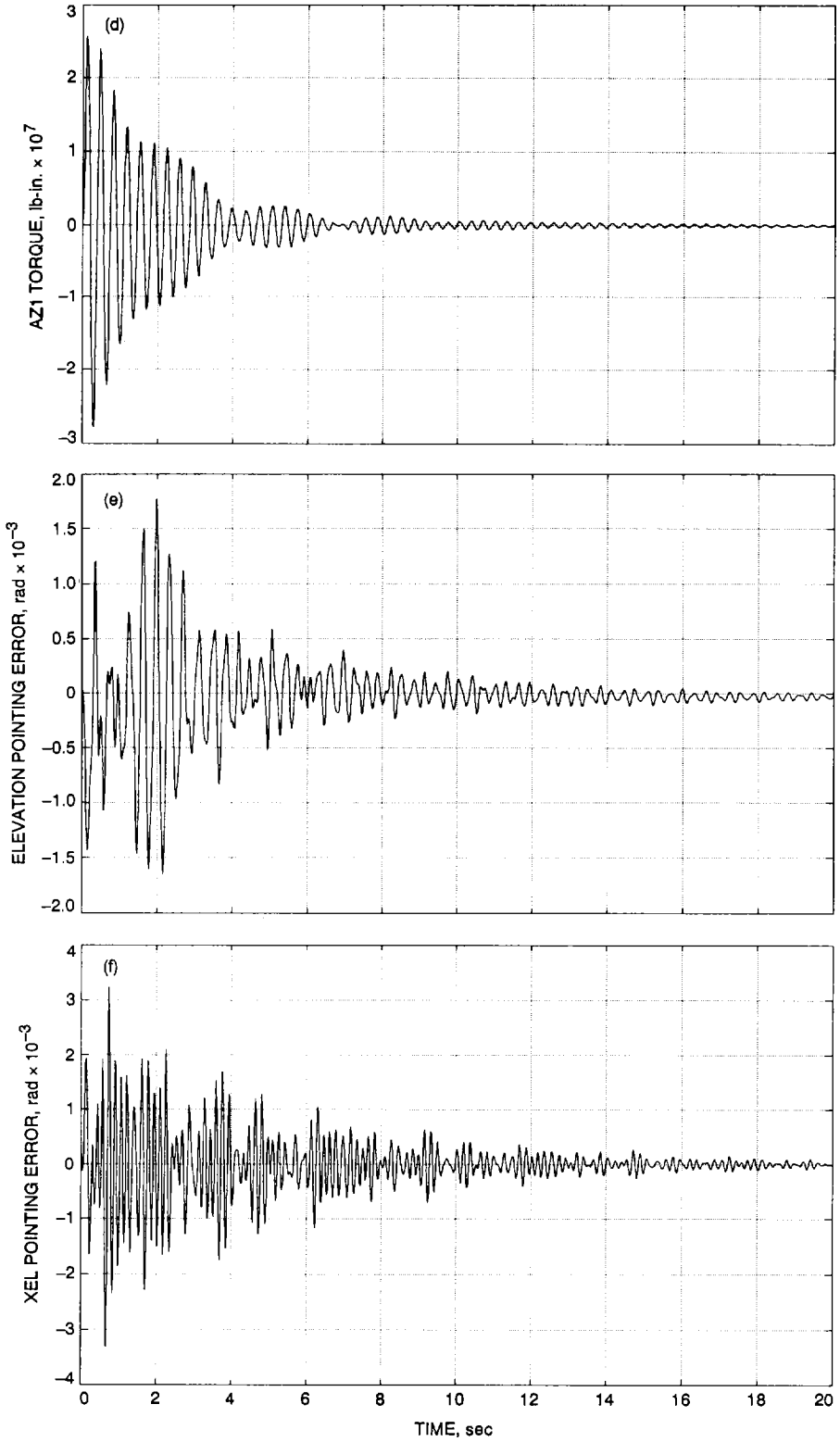
(d)
AZ1 TORQUE, lb-in. x 10^7
3
2
1
0
−1
−2
−3
(e)
ELEVATION POINTING ERROR, rad x 10^−3
2.0
1.5
1.0
0.5
0
−0.5
−1.0
−1.5
−2.0
(f)
XEL POINTING ERROR, rad x 10^−3
4
3
2
1
0
−1
−2
−3
−4
0
2
4
6
8
10
12
14
16
18
20
TIME, sec

Fig. 17 (contd).

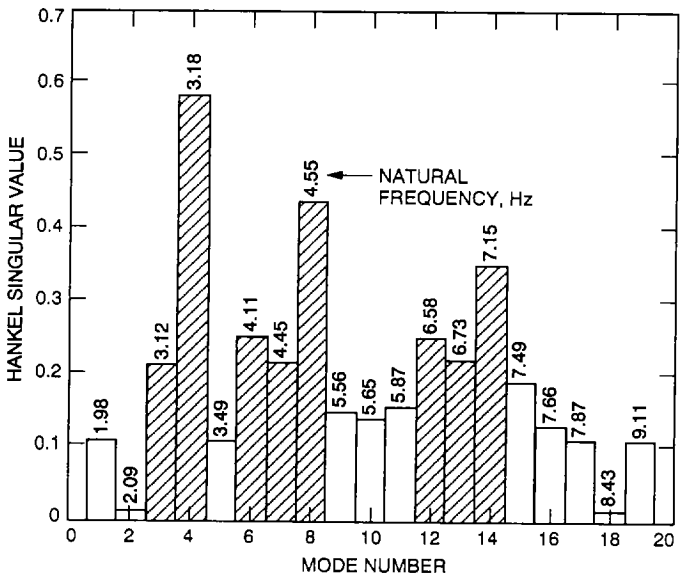

Fig. 18. Hankel singular values for the antenna structure with the wind input.

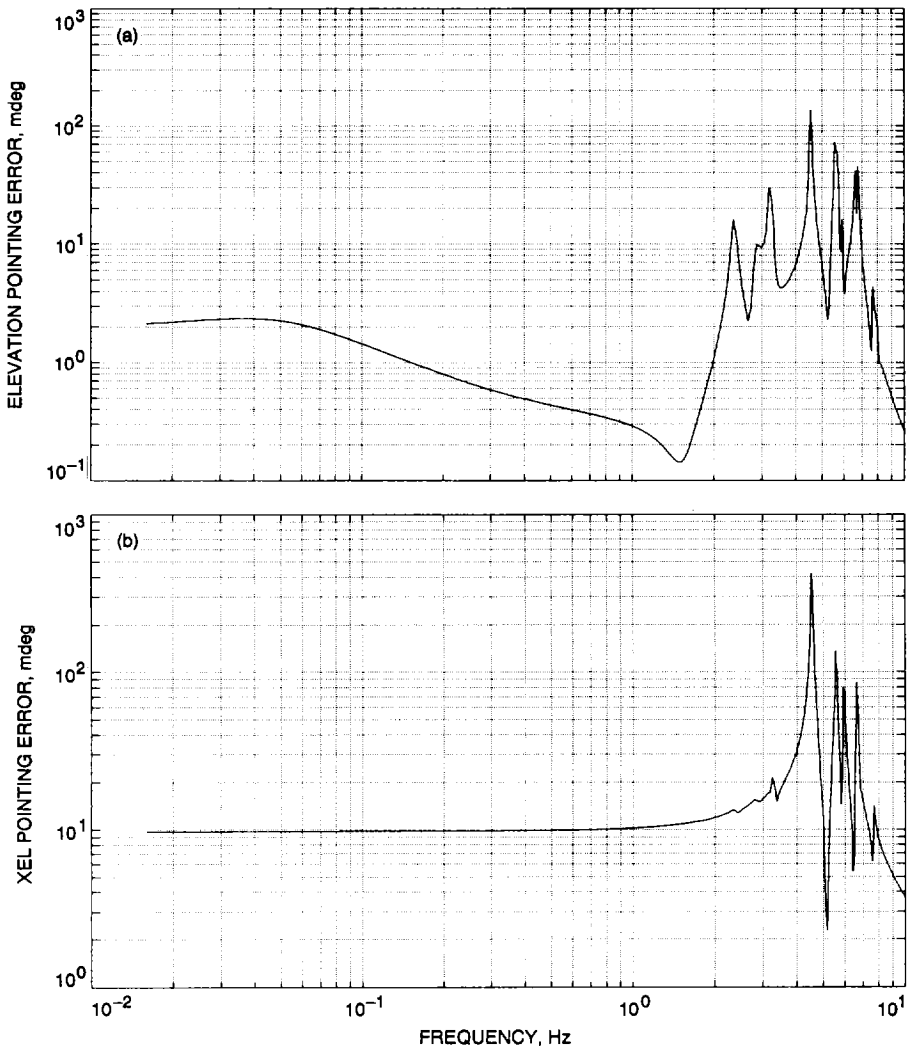

Fig. 19. Magnitudes of transfer functions of the closed-loop system: (a) from the wind force in *x*-direction to the elevation pointing error, (b) from the wind force in *x*-direction to the XEL pointing error, (c) from the wind force in *y*-direction to the elevation pointing error, and (d) from the wind force in *y*-direction to XEL pointing error.

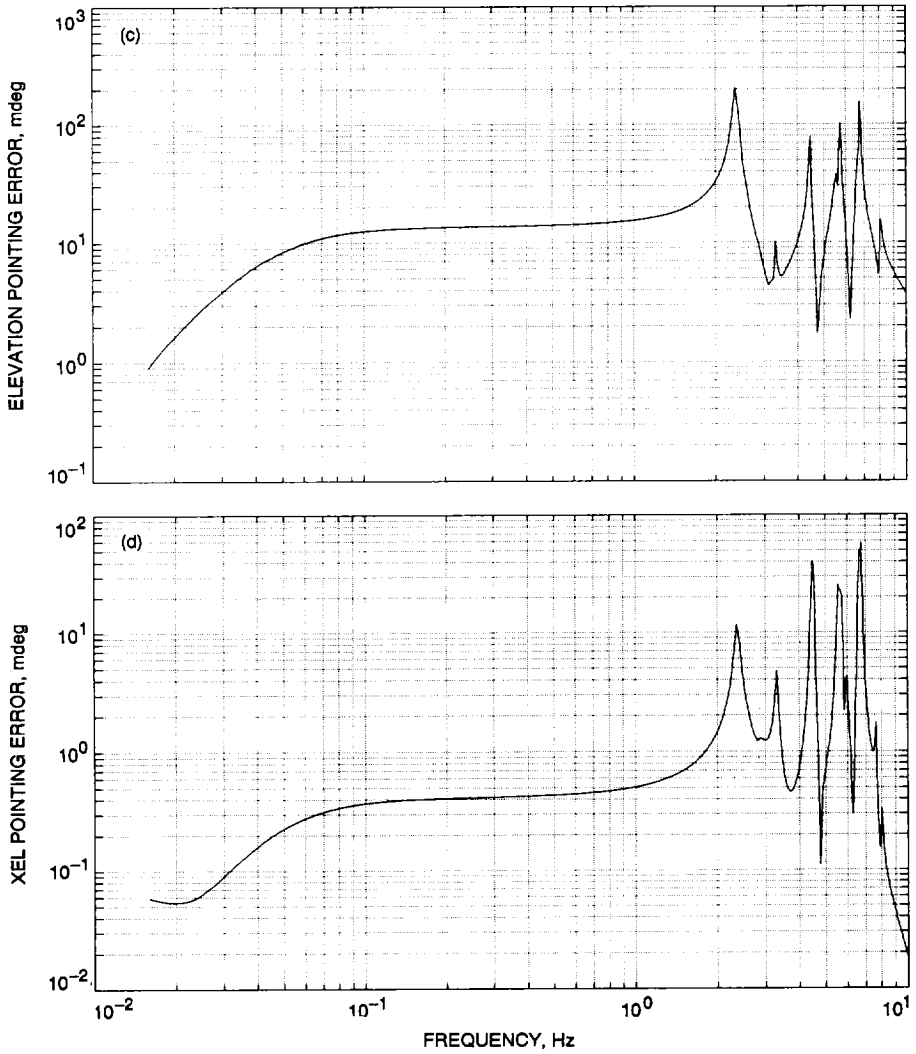
(c)
ELEVATION POINTING ERROR, mdeg
10^3
10^2
10^1
10^0
10^{-1}
(d)
XEL POINTING ERROR, mdeg
10^2
10^1
10^0
10^{-1}
10^{-2}
10^{-2}
10^{-1}
10^0
10^1
FREQUENCY, Hz

Fig. 19 (contd).

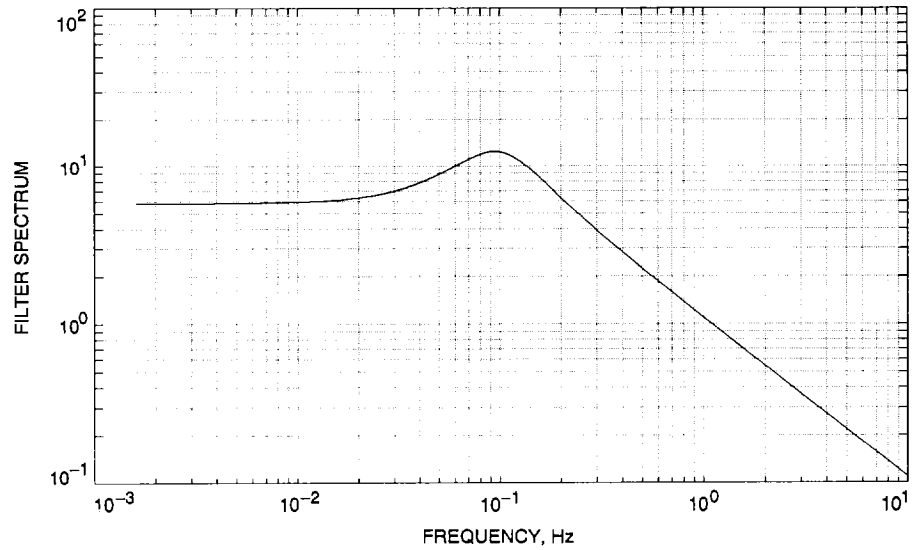

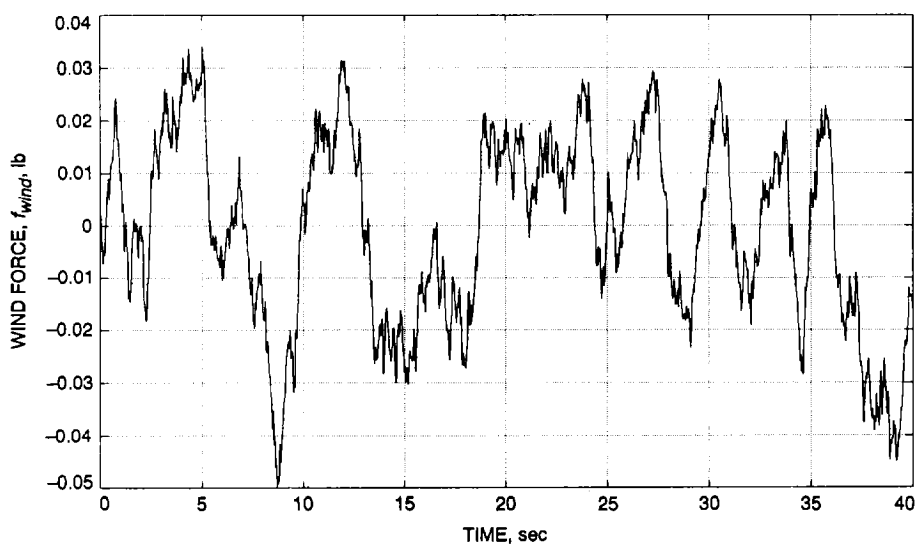

Fig. 21. Wind force acting on the tipping structure for wind 30 mph and with f_{max} = 0.1 Hz and rms (f_{wind}) = 0.18.

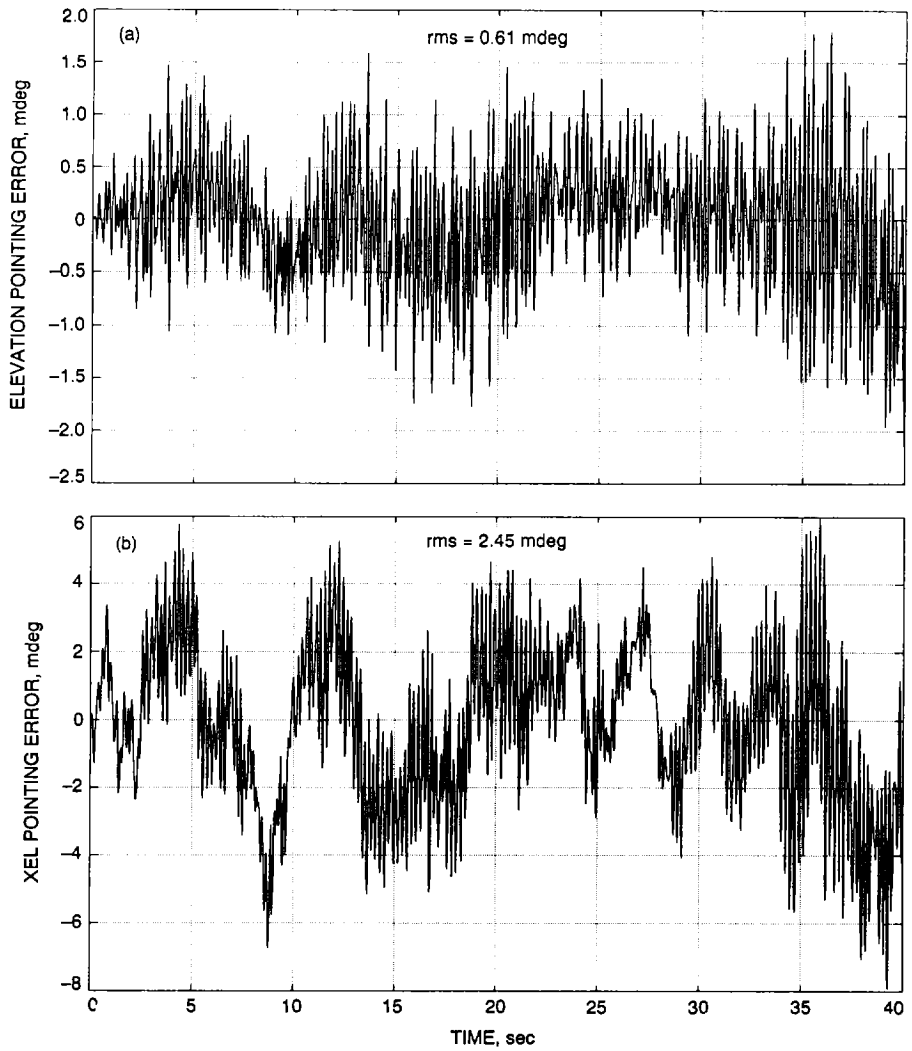

Fig. 22. Closed-loop antenna responses to 30 mph wind, f_{max} = 0.1 Hz, and rms (f_{wind}) = 0.18: (a) elevation pointing error, x-direction wind, (b) XEL pointing error, x-direction wind, (c) elevation pointing error, y-direction wind, and (d) XEL pointing error, y-direction wind.

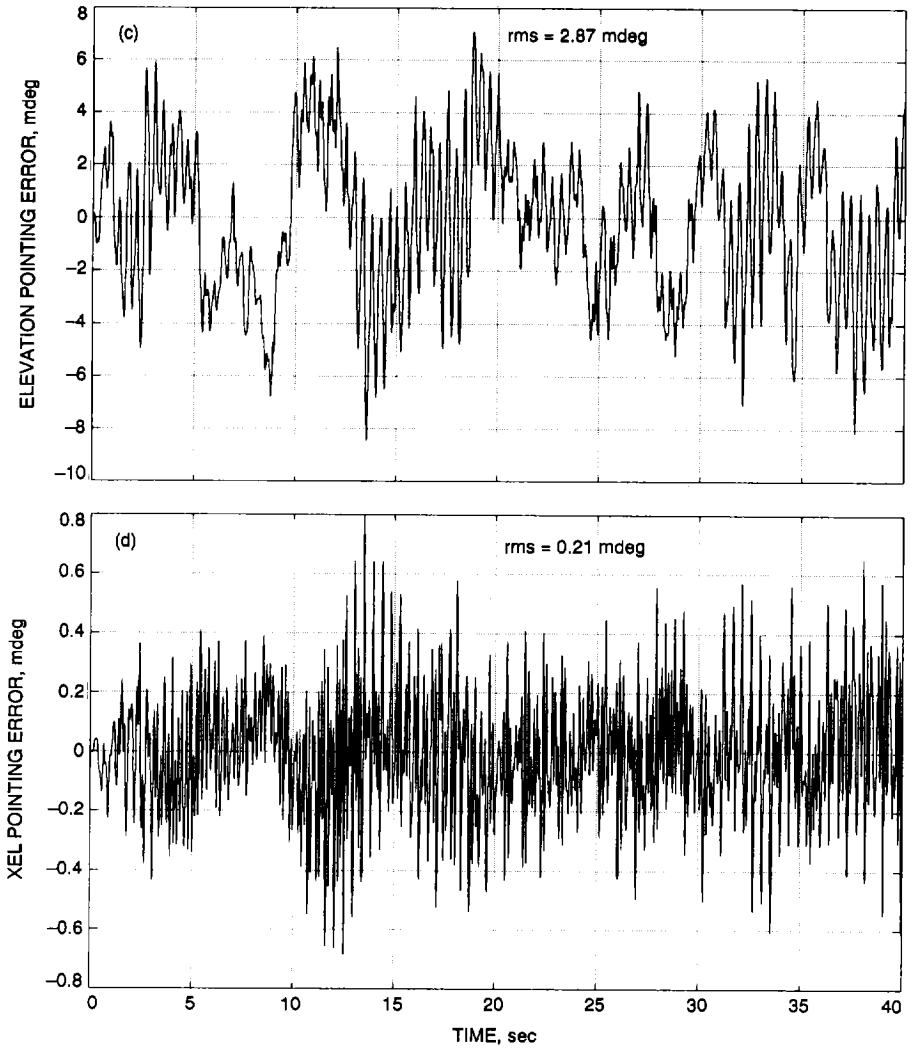
(c)
rms = 2.87 mdeg
ELEVATION POINTING ERROR, mdeg
8
6
4
2
0
−2
−4
−6
−8
−10
(d)
rms = 0.21 mdeg
XEL POINTING ERROR, mdeg
0.8
0.6
0.4
0.2
0
−0.2
−0.4
−0.6
−0.8
0
5
10
15
20
25
30
35
40
TIME, sec

Fig. 22 (contd).

Appendix A
Parameters of the DSS 13 Antenna

The structural parameters for the DSS 13 antenna are:

$\alpha = 25$ deg

$\zeta_i = 0.005$ for $i = 1, \cdots, 21$

node numbers are $nc = 5380, no = 86,302, nu = 86,881$, and $nb = 41,212$

$$\begin{aligned}\Omega = diag\ (\ & 0, & 0, & 12.4344, & 13.1067, & 19.6287, & 19.9805, & 21.9158, \\ & 25.8490, & 27.9288, & 28.6011, & 34.9094, & 35.5126, & 36.8760, & 41.3559, \\ & 42.3047, & 44.9499, & 47.0485, & 48.1292, & 49.4675, & 52.9547, & 57.2524)\end{aligned}$$

$$\begin{aligned}M_m = diag\ (\ & 214.3607, & 296.0889, & 692.2613, & 11.3445, & 244.8719, & 62.6765, & 65.7475, \\ & 799.5434, & 17.9187, & 18.6408, & 18.9721, & 24.6747, & 53.4131, & 7.8255, \\ & 9.7606, & 37.4093, & 38.2110, & 27.3915, & 25.5052, & 7.5668, & 200.0856)\end{aligned}$$

modal matrix $\Phi = [\phi_1, \phi_2, \cdots, \phi_{21}]$, where $\phi_i = i$th mode shape and $\phi_i = [\phi_{i1}, \phi_{i2}, \cdots, \phi_{ip}]^T$, where $\phi_{ij} = j$th component of the ith mode.

The rate-loop system parameters for the DSS 13 antenna are:

$k_1 = 716.197$ V sec/rad

$k_m = 15.72$ lb/A for elevation

$k_m = 15.36$ lb/A for azimuth

$k_b = 1.79$ V sec/rad

$k_s = 0.8$ V/V

$k_{tach} = 0.0384123$ V sec/rad for elevation

$k_{tach} = 0.037337$ V sec/rad for azimuth

$k_r = 80$ V/sec V for a range of 49–83

$k_i = 87.13$ V/sec V

$k_{iie} = k_{iia} = 0.1$

$k_{ppe} = k_{iia} = 0.5$

$k_{cur} = 0.12658$ V/A

$k_f = 54$ V/V

$k_{go} = 1.5 \times 10^7$ lb/rad for elevation

$k_{go} = 2.0 \times 10^7$ lb/rad for azimuth

$k_{ctfr} = 0.33$

$k_{ct} = 0.11111$

$k_{bs} = 0.66$

$\tau_1 = 0.0063662$ sec

$\tau_2 = 0.094$ sec

$\tau_3 = 0.002$ sec

$\tau_4 = 0.00484$ sec

$\tau_5 = 0.0021$ sec

$\tau_6 = 0.7304$ sec

$N = 354$ for elevation

$N = 595$ for azimuth

$J_m = 1.236$ lb/sec^2 for elevation

$J_m = 1.0848$ lb/sec^2 for azimuth

$R_a = 0.456\ \Omega$ for elevation

$R_a = 0.668\ \Omega$ for azimuth

$L_a = 0.011\ H$ for elevation

$L_a = 0.0144\ H$ for azimuth

Appendix B

Model Reduction for Systems With Integrators

Model order reduction methods for stable linear systems are based on joint controllability and observability tests, through balancing of system grammians [2]. For linear unstable systems, various techniques based on properties of the controllability and observability grammians have been developed [8,9,10]. Consider a system with integrators whose output is an integral of an input. It has a pole (or poles) at zero, consequently, its controllability and observability grammians do not exist, and model reduction based on its grammian properties cannot be executed. Systems with integrators, however, are controllable and observable, hence, these properties can still be used for model reduction. In this appendix the reduction algorithm for systems with integrators is derived, and systems with integrators are defined as follows.

Definition B.1. A linear system with the state-space representation (A, B, C, D), $A \in \Re^{n\times n}$, $B \in \Re^{n\times p}$, $C \in \Re^{q\times n}$, and $D \in \Re^{q\times p}$, is a system with integrators if its $n-m$ poles are stable, the remaining m poles are at zero, and it is observable and controllable, see [11]. It is assumed also that A is nondefective [12] (geometric multiplicity of poles at zero is m).

Systems with integrators are linear systems commonly encountered in control design and analysis. This appendix presents a reduction method, by introducing antigrammians.

Definition B.2. For a controllable and observable triple (A, B, C), the matrices V_c and V_o satisfying the following Riccati equations:

$$\left.\begin{aligned} V_cA + A^TV_c + V_cBB^TV_c = 0 \\ V_0A^T + AV_o + V_oC^TCV_o = 0 \end{aligned}\right\} \qquad \text{(B-1a)}$$

are the controllability and observability antigrammians.

For stable controllable and observable systems $V_o = W_c^{-1}$ and $V_o = W_o^{-1}$, where W_c and W_o are controllability and observability grammians and satisfy the Lyapunov equations

$$\left.\begin{aligned} AW_c + W_cA^T + BB^T = 0 \\ W_oA + A^TW_o + C^TC = 0 \end{aligned}\right\} \qquad \text{(B-1b)}$$

Note that the grammians for a system with integrators do not exist, but antigrammians do; for an unobservable or uncontrollable system antigrammians do not exist, but grammians do. The existence of antigrammians is exploited for the balancing and model reduction of systems with integrators.

For a stable, controllable, observable, and balanced system the grammians as well as the antigrammians are equal and diagonal

$$W_c = W_o = \Gamma, V_c = V_o = \Pi, \qquad \Pi = \Gamma^{-1} \qquad \text{(B-2)}$$

where $\Gamma = diag(\gamma_i)$ and $\Pi = diag(\pi_i)$ for $i = 1, 2, \ldots, n$, and satisfy the following equations:

$$\left.\begin{aligned} \Pi A_b + A_b^T\Pi + \Pi B_bB_b^T\Pi = 0 \\ \Pi A_b^T + A_b\Pi + \Pi C_b^TC_b\Pi = 0 \end{aligned}\right\} \qquad \text{(B-3a)}$$

$$\left.\begin{aligned} A_b\Gamma + \Gamma A_b^T + B_bB_b^T = 0 \\ \Gamma A_b + A_b^T\Gamma + C_b^TC_b = 0 \end{aligned}\right\} \qquad \text{(B-3b)}$$

The representation (A_b, B_b, C_b, D) is balanced.

Proposition B.1. For a balanced system with integrators one obtains $\Pi = diag(0_m\ \Pi_o)$, where 0_m is an $m \times m$ zero matrix, and A_b is block-diagonal, $A_b = diag(0_m\ A_{bo})$.

Proof. Consider A, B, and C in the form

$$A = diag(0_m\ A_o), \quad B^T = [B_r^T\ B_o^T], \quad C = [C_r\ C_o] \quad \text{(B-4)}$$

Matrix A in the form of Eq. (B-4) always exists due to m poles at zero, and B and C exist due to nondefectiveness of A. From Eq. (B-1a) it follows that:

$$V_{crr}B_r = 0, \quad C_rV_{orr} = 0, \quad V_{cro} = 0, \quad V_{oro} = 0 \qquad \text{(B-5)}$$

where V_c and V_o are divided conformably to A:

$$V_c = \begin{bmatrix} V_{crr} & V_{cro} \\ V_{cro}^T & V_{coo} \end{bmatrix}, \qquad V_o = \begin{bmatrix} V_{orr} & V_{oro} \\ V_{oro}^T & V_{ooo} \end{bmatrix}$$

For a controllable and observable system (by Definition B.1) the matrices B_r and C_r are of full rank, thus it follows from Eq. (B-5) that $V_{crr} = 0, V_{orr} = 0$, and that $V_c = diag(0_m \; V_{coo}), V_o = diag(0_m \; V_{ooo})$, which in balanced coordinates gives $\Pi = diag(0_m \; \Pi_o)$. ❐

Proposition B.2. A balanced representation of a system with integrators (A_b, B_b, C_b, D) is obtained by the transformation T_b

$$A_b = T_b^{-1} A T_b, \quad B_b = T_b^{-1} B, \quad C_b = C T_b \tag{B-6}$$

where

$$T_b = T_1 T_2 \tag{B-7}$$

The transformation T_1 turns A into block-diagonal form $A_1 = diag(0_m \; A_o)$, e.g., into real modal form

$$A_1 = T_1^{-1} A T_1 \tag{B-8}$$

and the transformation T_2 is represented by the form $T_2 = diag\ (I_m \; T_{bo})$, where I_m is an identity matrix of order m, and T_{bo} balances A_o

$$A_{bo} = T_{bo}^{-1} A_o T_{bo} \tag{B-9}$$

Proof. Immediate, by introducing Eq. (B-5) into Eq. (B-3a). ❐

The antigrammian Π of a balanced system with integrators is ordered increasingly

$$\Pi = diag(\pi_1, \pi_2, \ldots, \pi_{n-1}, \pi_n) \tag{B-10}$$

where $\pi_i \geq 0$ and $\pi_{i+1} \geq \pi_i$ for $i = 1, \ldots, n$, with the first m singular values at zero, $\pi_i = 0$ for $i = 1, \ldots, m$. The system is reduced by truncating the last $n-k$ states of the balanced representation and leaving its first k states. Let the matrices A_b, B_b, and C_b be partitioned conformably

$$A_b = \begin{bmatrix} A_{11} & A_{12} \\ A_{21} & A_{22} \end{bmatrix}, \quad B_b = \begin{bmatrix} B_1 \\ B_2 \end{bmatrix}, \quad C_b = [C_1 C_2] \tag{B-11}$$

then the reduced system representation (A_r, B_r, C_r, D_r) is $A_r = A_{11}, B_r = B_1, C_r = C_1$, and D remains unchanged. The system can also be reduced by the enhanced low-frequency approximation, see [13,14]

$$\left.\begin{aligned} A_r &= A_{11} - A_{12} A_{22}^{-1} A_{21}, \\ B_r &= B_1 - A_{12} A_{22}^{-1} B_2, \\ C_r &= C_1 - C_2 A_{22}^{-1} A_{21}, \\ D_r &= D - C_2 A_{22}^{-1} B_2 \end{aligned}\right\} \tag{B-12}$$